Integral field spectroscopy of planetary nebulae: mapping the line diagnostics and hydrogen-poor zones with VLT FLAMES

Journal Item

Mon. Not. R. Astron. Soc. **386,** 22–46 (2008) doi:10.1111/j.1365-2966.2008.13051.x

Integral field spectroscopy of planetary nebulae: mapping the line diagnostics and hydrogen-poor zones with VLT FLAMES⋆

Y. G. Tsamis,[1,2]† J. R. Walsh,[2] D. Péquignot,[3] M. J. Barlow,[1] I. J. Danziger[4] and X.-W. Liu[5]

[1]*Department of Physics and Astronomy, University College London, Gower Street, London WC1E 6BT*
[2]*Space Telescope European Co-ordinating Facility, European Southern Observatory, Karl-Schwarzschild Strasse 2, D-85748 Garching, Germany*
[3]*LUTH, Observatoire de Paris, CNRS, Université Paris Diderot; 5 Place Jules Janssen, 92190 Meudon, France*
[4]*Osservatorio Astronomico di Trieste, Via G. B. Tiepolo 11, I-34131 Trieste, Italy*
[5]*Department of Astronomy, Peking University, Beijing 100871, China*

Accepted 2008 January 28. Received 2008 January 17; in original form 2007 December 6

ABSTRACT

Results from the first dedicated study of Galactic planetary nebulae (PNe) by means of optical integral field spectroscopy with the Very Large Telescope Fibre Large Array Multi Element Spectrograph Argus integral field unit are presented. Three typical Galactic disc PNe have been mapped with the 11.5×7.2-arcsec^2 Argus array: 2D spectral maps of the main shell of NGC 5882 and of large areas of NGC 6153 and NGC 7009 with 297 spatial pixels per target were obtained at subarcsec resolutions. A corresponding number of 297 spectra per target were obtained in the 396.4–507.8 nm range. Spatially resolved maps of emission lines and of nebular physical properties such as electron temperatures, densities and ionic abundances were produced. The abundances of helium and of doubly ionized carbon and oxygen, relative to hydrogen, were derived from optical recombination lines (ORLs), while those of O^{2+} were also derived from the classic collisionally excited lines (CELs). The occurrence of the abundance discrepancy problem, pertaining to oxygen, was investigated by mapping the ratio of ORL/CEL abundances for O^{2+} [the abundance discrepancy factor (ADF)] across the face of the PNe. The ADF varies between targets and also with position within the targets, attaining values of ∼40 in the case of NGC 6153 and ∼30 in the case of NGC 7009. Correlations of the ADF with geometric distance from the central star and plasma surface brightness (for NGC 6153), as well as with [O III] electron temperature, plasma ionization state and other physical properties of the targets are established. Very small values of the temperature fluctuation parameter in the plane of the sky, $t_A^2(O^{2+})$, are found in all cases.

It is argued that these results provide further evidence for the existence in run-of-the-mill PNe of a distinct nebular component consisting of hydrogen-deficient, super-metal-rich plasma. The zones containing this posited component appear as undulations in the C II and O II ORL abundance diagnostics of about 2 spatial pixels across, and so any associated structures should have physical sizes of less than ∼1000 astronomical units. Regarding the origin of the inferred zones, we propose that circumstellar discs, Abell 30-type knots, or Helix-type cometary globules may be involved. Implications for emission-line studies of nebulae are discussed.

Key words: ISM: abundances – planetary nebulae: general – planetary nebulae: individual: NGC 5882 – planetary nebulae: individual: NGC 6153 – planetary nebulae: individual: NGC 7009.

⋆Based on observations made with ESO telescopes at the Paranal Observatory under programme ID 075.D-0847(A).

†E-mail: ygt@star.ucl.ac.uk

1 INTRODUCTION

Planetary nebulae (PNe) represent only an ephemeral stage in the late evolution of low- to intermediate-mass stars, the predominant stellar population in late-type galaxies, but their rich emission-line spectra allow us to quantify the amounts of helium, and heavier elements (mainly carbon, nitrogen, and *s*-process elements) that these stars produce and return into the interstellar medium. Recent studies have indicated that PNe may also contain non-negligible amounts of endogenous oxygen and neon synthesized by intrinsic nucleosynthesis in the stellar progenitors and expelled into the nebulae following the third dredge-up, especially more so in lower metallicity environments such as those of the Galactic Halo (Péquignot & Tsamis 2005) and of satellites of the Galaxy (Péquignot et al. 2000; Leisy & Dennefeld 2006; Zijlstra et al. 2006). Their importance as vital sources of neutron-capture elements, such as for instance selenium and krypton among others, is now observationally confirmed (Péquignot & Baluteau 1994; Sterling, Dinerstein & Kallman 2007). With the advent of 8-m class telescopes, PNe are increasingly being used as probes of the chemical evolution of Local Group galaxies (e.g. Gonçalves et al. 2007; Saviane et al. 2008), while by virtue of their intrinsically bright monochromatic [O III] 500.7 nm emission they have been detected in the intracluster stellar population of the Coma cluster at a distance of 100 Mpc (Gerhard et al. 2005, 2007).

A focal problem, however, remains in the astrophysics of these objects: namely that large discrepancies are measured between abundances and temperatures obtained from recombination lines and continua *versus* those obtained from the bright forbidden lines (e.g. Liu et al. 2000, 2004; Tsamis et al. 2003b, 2004; Wesson, Liu & Barlow 2005). For the majority of more than 100 PNe surveyed thus far by long-slit (or échelle) spectroscopy, abundances of the elements carbon, oxygen, nitrogen and neon derived from their optical recombination lines (ORLs) are higher than those derived from the classic ('forbidden') collisionally excited lines (CELs) by factors of 2–3 (see review by Liu et al. 2006, and references therein). For about 5–10 per cent of the surveyed objects, however, the discrepancies are in the 4–80 range, with the most pathological case to date being Hf 2-2 (Liu et al. 2006), a southern PN. In the cases of carbon, nitrogen (Tsamis 2002; Tsamis et al. 2004) and oxygen (Liu et al. 2001; Tsamis et al. 2004), large metal overabundances are correlated with lower plasma temperatures derived from ORLs and continua than from forbidden lines. The resolution of this problem remains of high priority as it continues to undermine our trust on secure elemental abundance determinations for PNe, and for other types of emission-line objects (such as H II regions; e.g. Tsamis et al. 2003a).

In the overwhelming majority of cases, the ratio of ORL/CEL abundances for a given heavy element ion [the abundance discrepancy factor (ADF)] is not correlated with the excitation energies, $E_{\rm ex}$, of the CELs involved: meaning that, per individual PN, infrared (IR) or ultraviolet/optical CELs of low and high $E_{\rm ex}$, respectively, yield very comparable ionic abundances, which are uniformly lower than the corresponding abundances of the same ions derived from ORLs. The most likely explanation for these spectroscopic results was judged to be the presence of cold plasma regions embedded in the nebular gas in the form of relatively dense, hydrogen-poor condensations – clumps or filaments (Liu et al. 2000; Tsamis 2002; Tsamis et al. 2004). Due to their elevated content in heavy elements (several times solar), these plasma regions would have reached photoionization equilibrium at lower temperatures than the ambient 'normal' composition gas by emitting far-IR lines, the primary nebular thermostat in relatively low temperatures. Since the emissivity of heavy element recombination lines is enhanced at lower temperatures, while at the same time that of the classic forbidden lines is diminished, the hydrogen-poor, heavy element-rich clumps would emit heavy element recombination lines profusely, yielding a truer estimate of the heavy element content of these regions.

Whereas the long-slit surveys yielded concrete evidence for elevated recombination-line abundances, the temperature of the suspected hydrogen-deficient clumps was tougher to determine since the diagnostic lines involved are faint and often suffer from blends in lower resolution spectra. Nevertheless, there has been evidence from those studies for temperatures lower by several thousand K than the typical CEL temperatures of photoionized nebulae (Liu et al. 2004; Tsamis et al. 2004). This is one aspect of the proposed 'dual abundance model' solution that renders it self-consistent, something rather lacking from alternative propositions, such as small-scale temperature fluctuations in a chemically homogeneous medium (e.g. Peimbert et al. 2004), which do not invoke a physical process to explain the discrepancies. A major unresolved issue remains the as-yet-unknown origin of the high-abundance clumps, and their mass relative to the total ionized nebular gas.

Heavy element recombination lines in nebulae can be a thousand times or more fainter than hydrogen recombination lines, in sharp contrast to the luminous forbidden lines emitted by the same heavy ions. We therefore brought to bear on this thorny issue the combination of integral field spectroscopy (IFS) and the light collecting power of the Very Large Telescope (VLT). IFS techniques allow spectra to be obtained from every spatial element in a 2D field of view, combined with imaging capability of the field at any wavelength across a given λ range. This is usually achieved by means of an integral field unit (IFU) array composed of microlenses coupled to optical fibres or slicers (e.g. Allington-Smith 2006). These are fed into a spectrograph and are subsequently individually imaged on the focal plane of the telescope.

The contiguous array of microlenses (or spatial pixels – 'spaxels') can also be thought of as a series of long-slits stacked together and, in this sense, an IFU of $m \times n$ spaxels used on a single telescope is equivalent to using an array of m telescopes equipped with long slits of n pixels each. It could be argued that in the former case a given observing programme is executed m times faster than when using a classic long-slit spectrograph. In reality, this is not strictly true as invariably there are some light losses associated with IFU fibres and their optical connection to the spectrograph (particularly at the interfaces with the microlenses and the feed into the slit). Overall, IFU observations afford considerable advantages especially in a science programme like ours where faint diagnostic lines are targeted, and where 2D mapping of nebular regions is sought in the hope of isolating suspect metal-rich regions which may a priori have a random spatial distribution in the nebula.

In addition, IFS data can provide the much-needed input to fully realize the capabilities of new plasma codes such as those developed in recent years for the 3D modelling of photoionized nebulae (e.g. Ercolano et al. 2003; Morisset, Stasińska & Peña 2005). For example, such codes can produce simulated 3D or 2D spectral images of model nebulae at arbitrary wavelengths and inclinations that can be readily evaluated using images obtained by IFS. Moreover, high spectral resolution IFS data such as those we obtained for NGC 7009 (Walsh et al., in preparation) can yield detailed information on the velocity field of an object that could allow a 3D kinematical model to be built. These are some of the wider aspects of this work.

Here, we pursue a physicochemical analysis of three representative PNe belonging to the Galactic disc population with published oxygen ADFs ranging from ∼2–10. Long-slit spectroscopy of the

targets has been published: NGC 5882 (Tsamis et al. 2003b, 2004); NGC 6153 (Liu et al. 2000); NGC 7009 (Liu et al. 1995, hereafter LSBC). In those studies, the first two targets were observed with a long slit scanned across the whole nebular surface. This technique, which was applied throughout the long-slit surveys, yielded *mean* relative emission-line fluxes for the whole PNe, but naturally any variations in the physical properties in the direction perpendicular to the slit could not be sampled. An analysis along an NGC 6153 fixed slit sampling a 'slice' of the nebula revealed substantial variations in the physical properties over the slit length. Typically, however, the formerly employed ∼2 arcsec wide slits achieved a rather coarse spatial sampling of ∼1.6 arcsec per pixel, without sampling the seeing which was of the order of 1 arcsec.

We obtained contiguous 2D spatial coverage of these PNe at subarcsec resolution with the Fibre Large Array Multi Element Spectrograph (FLAMES)/Giraffe IFU Argus. Our main aim was to map out the nebular properties and their variations across large nebular areas and to investigate in detail the existence of any heavy element-rich nebular regions, so as to place constraints on models that have been put forward to explain this astrophysical quandary. The sample PNe were chosen because NGC 6153 and NGC 7009 exhibit the abundance anomaly problem to a high degree (with known oxygen ADFs of ∼10 and 5, respectively) and are excellent cases for a detailed study, whereas NGC 5882 (with an ADF of ∼2) was meant to be our 'control' target as it represents the majority of Galactic nebulae that show a moderate degree of abundance discrepancies. The layout of this paper is as follows. The specifications of the observational data set are discussed in Section 2, the data-reduction methods are presented in Section 3, and the results in Sections 4 and 5. The discussion and our conclusions appear in Section 6. An introduction to this study was presented by Tsamis et al. (2007).

2 OBSERVATIONS

Integral field spectra of NGC 5882, NGC 6153 and NGC 7009 were obtained in service mode between 2005 March–June in subarcsec seeing with the FLAMES/Giraffe Argus IFU on the 8.2-m VLT UT2/Kueyen (P.I. Tsamis; ESO Period 75). The observing log is presented in Table 1. All targets were observed in the 396.4–507.8 nm range with the large 11.5 × 7.2-arcsec^2 IFU. The Argus unit is a rectangular array of 22 × 14 microlenses fed by optical fibres: the 11.5 × 7.2-arcsec^2 array thus projects 308 spaxels on the sky; the individual spaxel size is 0.52 × 0.52 arcsec^2. Eight spaxels are reserved for sky subtraction purposes (from a total of 14 dedicated sky fibres) and three presently correspond to broken fibres (appearing in the second row of a reconstructed Argus image; see Fig. 6); the remainder provide 297 individual spectra per target. The Giraffe spectrograph is equipped with a 2048 × 4096 EEV CCD which has 15 μm pixels. Two separate wavelength ranges were observed using the LR02 (3964–4567 Å) and LR03 (4501–5078 Å) grating set-ups. The respective spectral resolving powers, R (= λ/Δλ), were 10 200 and 12 000. Higher spectral resolution HR04 and HR06 spectra (R = 32 500) of NGC 7009 were also taken with the small 6.6 × 4.2-arcsec^2 IFU and will be published in a separate paper (Walsh et al., in preparation). Total exposure times were 6930 s (NGC 5882), 24 000 s (NGC 6153) and 4260 s (NGC 7009); more time was devoted to NGC 6153 than to the other two targets since this nebula has the lowest surface brightness, and exhibits the abundance anomaly to a high degree. The average seeing during the NGC 5882 exposures was 0.6 arcsec full width at half-maximum (FWHM); during six out of 10 observing blocks of NGC 6153 it was better than 0.8 arcsec, while during the remaining four it was ∼0.9 arcsec. During the NGC 7009 exposures, the seeing ranged between 0.5 and 0.8 arcsec. The sky transparency conditions were generally in the 'clear' category.

Table 1. Journal of VLT 8.2-m FLAMES Argus observations.

Target	Date (UT)	λ-range (Å)	Grating	Exposure time (s)
NGC 5882	23/03/05	3964–4567	LR02	3 × 440
	23/03/05	4501–5078	LR03	3 × 330
	29/04/05	3964–4567	LR02	6 × 440
	29/04/05	4501–5078	LR03	6 × 330
NGC 6153	29/04/05	3964–4567	LR02	6 × 800
	29/04/05	4501–5078	LR03	6 × 400
	30/04/05	3964–4567	LR02	12 × 800
	30/04/05	4501–5078	LR03	12 × 400
	01/05/05	3964–4567	LR02	4 × 800
	01/05/05	4501–5078	LR03	4 × 400
NGC 7009	02/06/05	3964–4567	LR02	8 × 270
	02/06/05	4501–5078	LR03	12 × 175

The positions observed on each PN were given due consideration. In Figs 1–3, we show the exact positions observed by overlaying Argus spectral images taken in the light of Hβ 4861 Å on *Hubble Space Telescope* (*HST*) WFPC2 images of the nebulae. The Argus maps have been drawn to scale in all cases. Regarding NGC 5882 (Fig. 1), which is the nebula with the smallest apparent size of the three, the IFU array was positioned so that the largest part of the bright shell of the PN as well as part of the fainter halo to the south could be covered. The centre of the IFU was positioned at $\alpha = 15^{\rm h}16^{\rm m}49\overset{\rm s}{.}8$, $\delta = -45^\circ39'01\overset{''}{.}4$ (J2000).

For NGC 6153 (Fig. 2), we chose to align the large axis of Argus roughly along the minor axis of the PN so as to cover both the bright patch visible on the *HST* image in the south-eastern outskirts of the nebula and the inner fainter regions closer to the central star – this position also shares the orientation of the 2-arcsec-wide fixed long slit employed by Liu et al. (2000). The centre of the IFU was positioned at $\alpha = 16^{\rm h}31^{\rm m}31\overset{\rm s}{.}0$, $\delta = -40^\circ15'12\overset{''}{.}4$ (J2000).

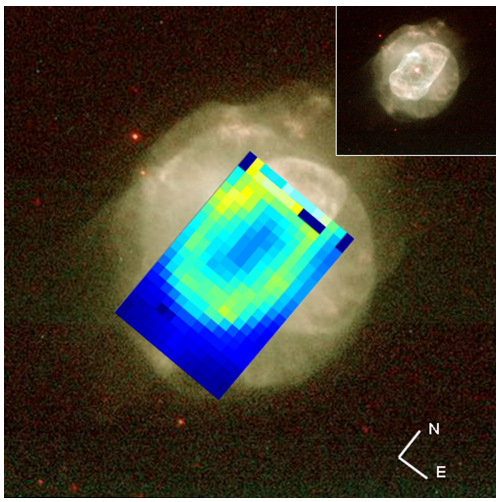

Figure 1. NGC 5882: VLT Argus Hβ map overlaid on a *HST* WFPC2 image of the nebula covered by the 11.5 × 7.2-arcsec^2 IFU. The *HST* snapshot was taken with a broad-band *F555W* filter (credit: H. Bond and Space Telescope Science Institute). The position of the stellar nucleus is visible in the inset.

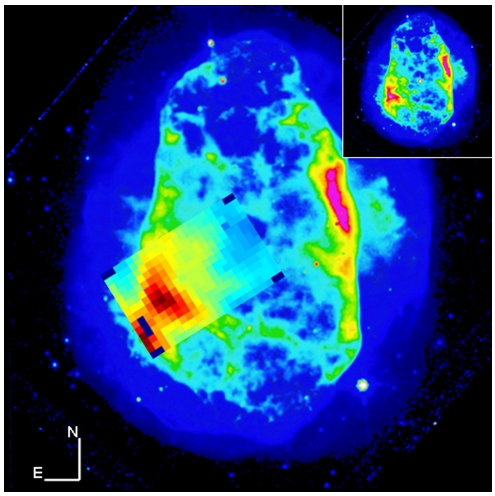

Figure 2. NGC 6153: VLT Argus Hβ map overlaid on a pseudo-colour *HST* WFPC2 broad-band filter *F814W* image of the nebula covered by the 11.5 × 7.2-arcsec^2 IFU (source of *HST* image: Liu et al. 2000). The position of the stellar nucleus is visible in the inset.

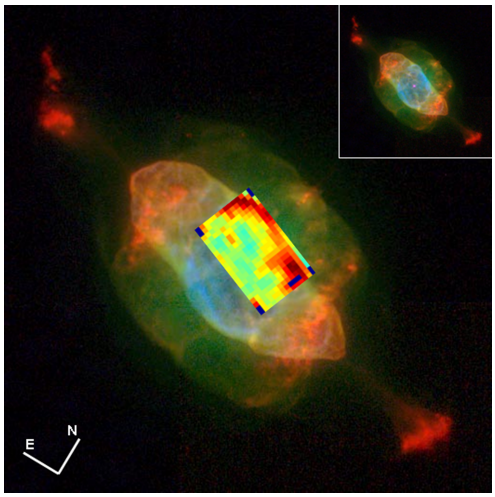

Figure 3. NGC 7009: VLT Argus Hβ map overlaid on a *HST* WFPC2 image outlining the area of the nebula covered by the 11.5 × 7.2-arcsec^2 IFU. The *HST* pseudo-colour is a composite of *F658N* = [N II] (red), *F502N* = [O III] (green) and *F469N* = He II (blue) frames (credit: B. Balick and Space Telescope Science Institute). The position of the stellar nucleus is seen in the inset.

NGC 7009 (Fig. 3) has an elliptical shape with low-ionization emission regions at both ends of its major axis of symmetry which give it a bipolar appearance. It shows a clearly defined bright inner shell surrounded by a fainter outer envelope. We thus chose to place the IFU array so that both the faint regions in the centre of the PN and the sharp rim of the bright inner shell could be covered. The centre of the IFU was positioned at $\alpha = 21^{\rm h}04^{\rm m}10\overset{\rm s}{.}8$, $\delta = -11^\circ21'48\overset{''}{.}7$ (J2000). In all cases, the central stars of the PNe (visible in the insets of the *HST*/Argus overlays) fell within the IFU field of view and were a useful point of reference. This further allowed us to examine the nebular physical conditions in the immediate vicinity of the stellar nuclei.

3 DATA REDUCTION

The spectra were reduced at ESO Garching with the girBLDRS pipeline[1] in a process which included bias removal, localization of fibres on the flats, extraction of individual fibres, wavelength calibration and rebinning of the Th–Ar lamp exposures, and the full processing of the science frames which resulted in cosmic-ray cleaned, flat-fielded, wavelength-rebinned spectra. In practice, the pipeline actions were initiated by the creation of a master bias frame from the raw biases (BIASMAST pipe) which was subtracted from the science exposures at a later reduction step. The localization of fibres on the flat field frames followed (LOCMAST pipe). The full master wavelength solution was produced via the extraction, wavelength calibration and rebinning of the raw Th–Ar exposures (WCALMAST pipe). This was followed by the full processing of the science frames via the EXTRACT recipe which, by using the products of the previous steps, subtracts the master bias from the science exposures, takes out an average rejecting any cosmic ray hits, performs the flat-fielding, and finally rebins the extracted spectra in wavelength space. In this way, four to six science frames per observing block were processed together and the resulting frame was corrected for atmospheric extinction within IRAF. The airmass during the exposures was ∼1.1. When this varied by more than ∼0.1 during the course of a single observing block (1 h) the frames were extracted individually and were corrected for atmospheric extinction one at a time. They were subsequently averaged using the IMCOMBINE task which performed the cosmic ray rejection as well. The flux calibration was achieved using exposures of the white dwarf EG 274 using the tasks CALIBRATE and STANDARD. The flux standard exposures were first individually extracted with girBLDRS and the spaxels containing the star were summed up to form a 1D spectrum. The sensitivity function was determined using IRAF's SENSFUNC and this was subsequently applied to the combined science exposures. The sky subtraction was performed by averaging the spectra recorded by the sky fibres and subtracting this spectrum from that of each spaxel in the IFU. Each of the 14 sky fibre spectra were examined and the average count in each compared. Four sky fibres had higher counts caused by contamination from the simultaneous calibration lamp (see below), and were not included in the computation of the mean sky spectrum.

Custom-made scripts allowed us to convert the row by row stacked, processed CCD spectra to data cubes. The nebular emission-line fluxes were generally measured automatically by fitting Gaussian profiles via means of the dedicated program SPECTRE which is based on MINUIT χ^2 minimization routines (James 1998). This enabled us to retrieve from the spectra associated with each spaxel: the line fluxes, the line FWHM, equivalent widths, line centroids, and the respective errors of these quantities which were propagated in all physical properties derived afterwards.[2] The same program was used to interactively fit the nebular lines in the vicinity of the PN nuclei, and the absorption lines underneath the H I lines over the same spaxels. In Figs 4 and 5, Giraffe spectra of the PNe from single spaxel extractions in the vicinity of 465.0 nm are shown, covering the full O II V1 recombination multiplet, a few N II and C III ORLs, N III Bowen fluorescence lines, and He II λ4686. The lower panels display the observed spectrum (black line), along with

[1] The girBLDRS pipeline is provided by the Geneva Observatory (http://girbldrs.sourceforge.net/).

[2] The pre-analysis errors produced by the pipeline were used as the starting point of the error analysis; they also include uncertainties from the flat-fielding and the geometric correction of the spectra and not just photon-noise (Blecha & Simond 2004).

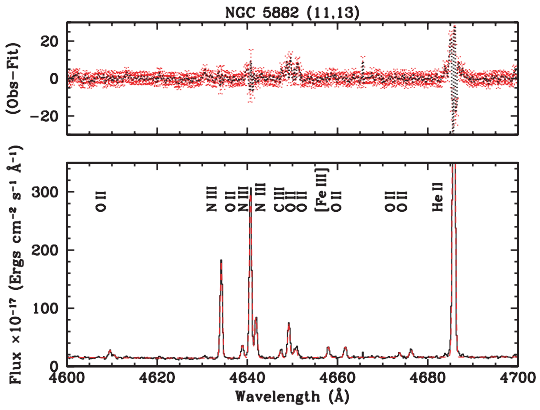

Figure 4. Spectrum of NGC 5882 from spaxel (11, 13) highlighting the O II V1 multiplet recombination lines. The red line is a sum of Gaussians plus a cubic spline continuum fit to the data (black line). The top panel shows the residuals of the fit (black) compared to the error bars of each point in the spectrum (red).

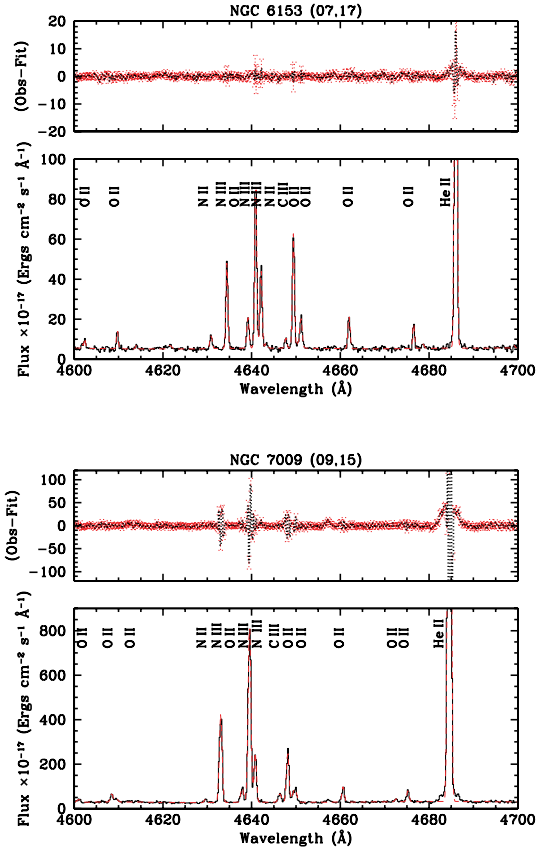

Figure 5. The same as Fig. 4 for NGC 6153 (top panel) and NGC 7009 (bottom panel).

the sum of the fitted continuum (cubic spline fit) and the individual Gaussians (red line). The upper panels show the errors bars at each point in the spectrum (red) and the residuals from the line and continuum fitting (black). In general, the fit residuals are comparable to the error bars. The fits in Figs 4–5 are for single Gaussian line fits to each emission species; for NGC 6153, 130 spaxels were fitted with double Gaussians, since the velocity splitting (due to nebular expansion) of 0.6 Å could be resolved by two lines of FWHM 0.5 Å. In the case of NGC 5882, 30 spaxels were fitted by double profiles.

The Gaussian fits to the brightest lines in Figs 4–5 show that the detailed profile deviates from a Gaussian and in the case of NGC 7009, for example, the very strong He II λ4686 line shows residuals in the line wings that are greater than the errors. Since only Gaussians were used for fitting, without a detailed line profile describing the grating scattering line wings, these line wing features were not fitted in detail. Neglect of these faint features constitutes a loss of less than one per cent to the line flux, and it was considered that a consistent line profile shape for all lines (i.e. Gaussian) was of highest priority for comparison of relative line fluxes (on which plasma conditions and abundance determinations that are central to this analysis depend). In general, the spectral resolution achieved was sufficient to resolve any known blends that affect heavy element ORLs in lower resolution spectra. Extra care was taken to interactively fit any remaining blended lines and to also fit double Gaussian profiles in cases where the spectral resolution was high enough to resolve the expansion of the nebula (e.g. in the case of NGC 6153).

An unforeseen issue arose due to the use of the 'simultaneous calibration lamp' during the science exposures. Use of this device is not really necessary for spectrophotometric work and it was left on unintentionally during the preparation of phase II. The lamp introduced an additive contamination pattern (Francesca Primas, private communication) on certain spaxels of the array (see Fig. 6), which showed up as a mix of broad and narrow features. All these features are light scattered from fibre to fibre and the broad features are presumably the scattering wings of strong lines in the comparison lamp spectrum. Since the PN line emission covered the whole of the IFU area for all three nebulae, there was no opportunity with the present data to subtract PN emission-free spaxel spectra in order to remove the contamination pattern. Instead, the contaminated spectra were interactively fitted by following the continuum in detail and any spurious narrower 'lines' were fitted by additional Gaussians. The results were satisfactory, although of course the fit errors on the nebular line fluxes were increased at those spaxels. The spectra of NGC 6153, which is the nebula with the lowest surface brightness, were most affected and 40 spaxels were interactively fitted and decontaminated in the manner described above.

Likewise, a scattered light feature appeared towards the last few CCD columns (long wavelengths) at the top-right corner of the

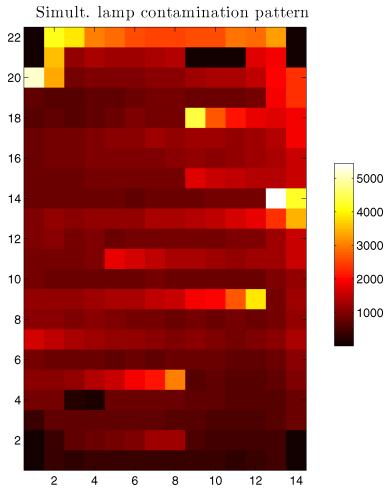

Figure 6. A spectral map of the continuum showing the characteristic pattern caused by contamination of the CCD from light leaking from the simultaneous calibration lamp of FLAMES. See the text for details.

stacked array. This was due to a residual CCD signal, which is a known cosmetic defect of the chip. The signal is additive (in excess of the bias) and, as it affected only certain spaxels in the reconstructed Argus image, it was fitted with a low-order polynomial and subtracted out. Finally, apart from the three fibres which were broken during ESO Period 75, the fibre corresponding to spaxel (4, 4)[3] of the reconstructed array is problematic in that it exhibits an anomalous spike in its signal, which often affected spaxels (3, 4) and (5, 4) too – the respective spectra were therefore handled accordingly and generally suffer from large uncertainties.

4 RESULTS

After the line fluxes had been measured, the reconstructed Argus data cubes were corrected for interstellar extinction using the $c(\mathrm{H}\beta)$ extinction maps derived from a comparison of the observed to the predicted $\mathrm{H}\gamma/\mathrm{H}\beta$ line ratio using its case B value from Storey & Hummer (1995). The Galactic extinction law of Howarth (1983) with a ratio of total to selective extinction (R_V) of 3.1 was used. Since the LR02 and LR03 spectra, containing the $\mathrm{H}\gamma$ and $\mathrm{H}\beta$ lines, respectively, were taken in different exposures, and often on different nights, it was necessary to tie the fluxes together in order to determine the extinction of the maps from the $\mathrm{H}\gamma$ to $\mathrm{H}\beta$ ratio. This comparison was performed by taking the total flux from the $\mathrm{H}\gamma$ and $\mathrm{H}\beta$ maps and comparing the ratio with that observed from long-slit studies. For NGC 5882, the absolute value of the ratio was taken as 0.410 from the scanned-slit (mean over the whole PN) data of Tsamis et al. (2003); for NGC 6153, the ratio for the whole nebula (0.333) was taken from Liu et al. (2000); for NGC 7009, the ratio of 0.443 for a value of $c(\mathrm{H}\beta) = 0.20$ was adopted (cf. LSBC). It should be noted that the IFU area does not exactly correspond to the comparison regions from the long-slit data, so the absolute extinction, and hence dereddened line ratios can be systematically offset. To gain an idea of the photometric quality of the observations, the LR02 and LR03 maps had to be corrected by 47, 5 and 5 per cent for NGC 5882, NGC 6153 and NGC 7009, respectively.

Potential shifts between the LR02 and LR03 maps, caused either by a slightly different pointing between the observations (although note that the LR02 and LR03 setting were always taken in pairs; Table 1) and/or the changing differential atmospheric extinction between the settings, were determined by cross-correlation of features in the $\mathrm{H}\gamma$ and $\mathrm{H}\beta$ maps. For NGC 5882, a shift of 0.25 spaxels in the IFU *X*-direction could be clearly detected (this PN has the sharpest spatial features as it was observed under ∼0.6 arcsec seeing). It was nonetheless decided not to correct the maps for this small shift since data at the IFU edges would be compromised. The extinction map for NGC 5882 does not show a very pronounced cusp at the position of the shell, as might be expected if the $\mathrm{H}\gamma$ and $\mathrm{H}\beta$ maps were poorly aligned.

In the paragraphs that follow, we present spectral maps for representative emission lines, the plasma physical conditions which were based on spectral map ratios, and the resulting chemical abundances.

4.1 Emission-line maps

4.1.1 NGC 5882

In Fig. 7, a set of NGC 5882 maps is presented showing the observed $\mathrm{H}\beta$, the logarithmic extinction at $\mathrm{H}\beta$, and a sample of representative dereddened spectral maps in the light of He I λ4471, He II λ4686, [O III] λ4959, [Ne III] λ3967, and the recombination lines C II λ4267 and O II λ4649. The top two rows of the array appear very bright in the 'unmasked' $\mathrm{H}\beta$ image: this does not appear in images of the other two PNe [except perhaps in spaxels (3–5, 22) for the brightest emission lines of NGC 6153] and was judged to be a combination of the effects of differential atmospheric extinction at the edge of the field of view and the fact that the line flux there shows quite a steep gradient – this is also evident from a comparison of our line map with the *HST F555W* image of the PN which shows a confluence of clumped, relatively high surface brightness emission in that area (Corradi et al. 2000). Such a gradient at the edge of the array could introduce errors in ratios of lines originating from the different LR02 and LR03 gratings and so these two rows were masked out and are not considered in the physical analysis of NGC 5882 that follows. We also decided to exclude the faint PN halo from a detailed analysis as the line signal-to-noise ratio (S/N) there, especially for the O II ORLs, was much lower than the IFU mean. A mask based on the $\mathrm{H}\beta$ S/N was therefore applied to exclude the halo region which appears with zero value spaxel intensities (coloured deep blue) in the $F(\mathrm{H}\beta)$ map of Fig. 7. Mean values of the physical conditions in the halo are given in Sections 4.2.1 and 4.3.1.

The emission lines peak on the main shell of NGC 5882 and especially on the north-west corner which coincides with the bright patch visible on the *HST* image (see inset of Fig. 1), our standard measure of comparison. The PN appears elliptical as in the *HST* image, and the southern portion of its halo is clearly registered in the 'unmasked' $\mathrm{H}\beta$ map. The south segment of its main shell appears faint in all lines and coincides with a low surface brightness blister-like feature on the *HST* image which extends towards the halo. The central regions are also much fainter relative to the main shell. The [O III] and [Ne III] maps appear very similar, as do the C II and O II ORL maps. He II λ4686 is more concentrated on the west part of the PN than on the east side, in contrast to the He I λ4471 emission which traces almost the full nebular ring. The dust extinction is variable across the nebula; $c(\mathrm{H}\beta)$ has a mean value of 0.449 ± 0.034 with an rms deviation of 0.241. Assuming a uniform interstellar extinction screen over the face of the PN, the central-eastern regions appear to be less dusty than the nebular shell.

4.1.2 NGC 6153

In Fig. 8, a set of NGC 6153 maps is presented showing the observed $\mathrm{H}\beta$, the logarithmic extinction at $\mathrm{H}\beta$, and a sample of representative dereddened spectral maps of metallic CELs, the helium recombination lines and the C II and O II ORLs. The Argus IFU targeted the brightest portion of the south-east quadrant of the nebula. The most striking feature in the maps is the high surface brightness patch peaking at around spaxel (8, 17) and which is clearly identified with the bright area in the south-eastern quadrant of the *HST* image (cf. Fig. 2). This area seems to have lower than average dust extinction associated with it, at $c(\mathrm{H}\beta) \simeq 0.9$ – the extinction is relatively higher towards the inner part of the nebula, and in the vicinity of the central star, with values closer to 1.3. The variations may not be very significant statistically; $c(\mathrm{H}\beta)$ has a mean value of 1.146 ± 0.180 with an rms deviation of 0.120. A lower surface brightness discontinuity is present in the bright area at coordinates ∼(5, 14) in all emission lines except [Ar IV] λ4711 (which appears bright over a large region). This discontinuity can be identified with the 'thinning' of the bright patch towards the north-east, something also seen in the inset of Fig. 2. He I λ4471 covers the same area of the IFU

[3] (*X*, *Y*) spaxel coordinates in the text are measured, respectively, on the minor-axis and major-axis of the Argus IFU; see Fig. 6.

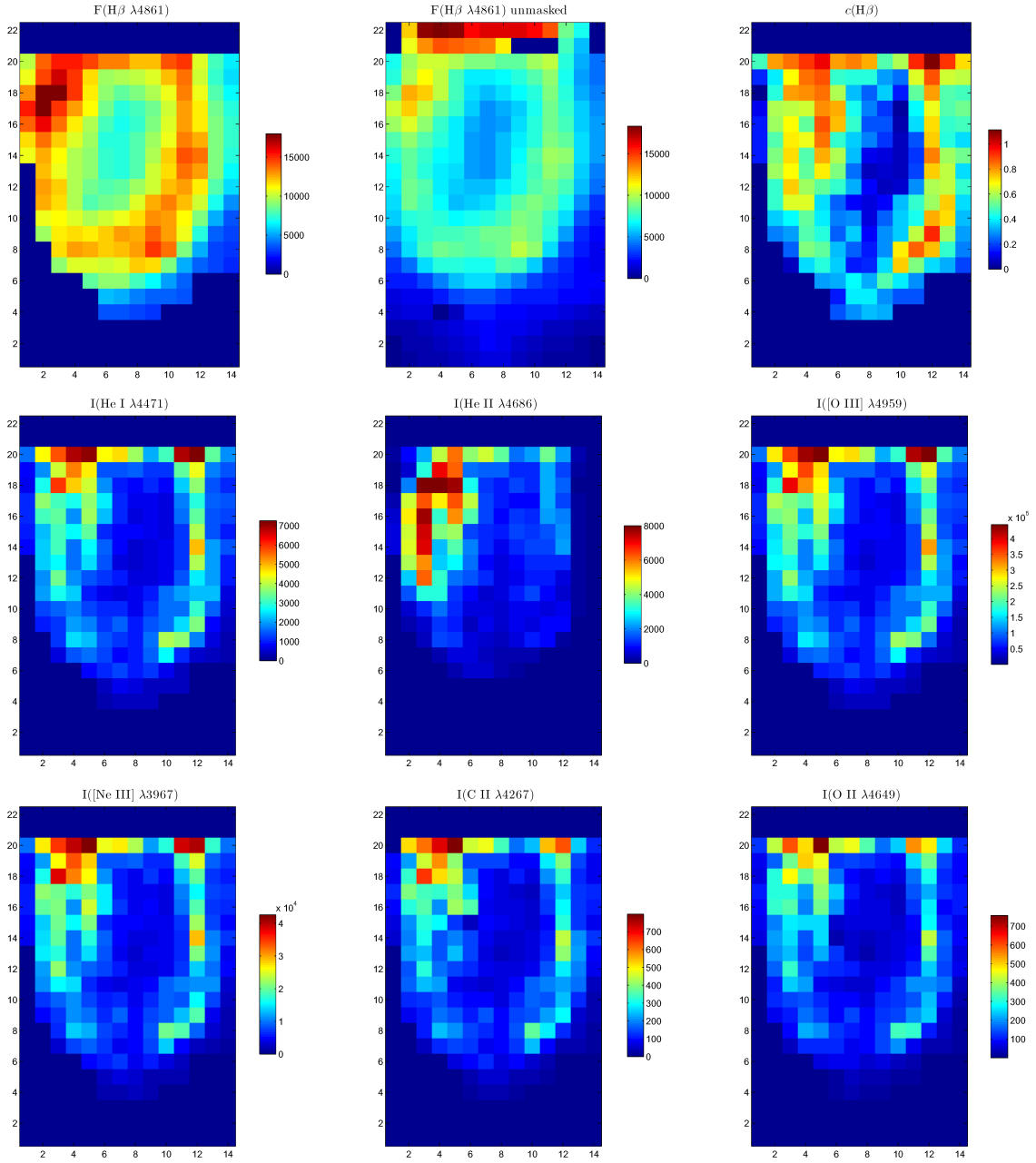

Figure 7. NGC 5882 monochromatic line flux (F) and dereddened intensity (I) maps (in units of 10^{-17} erg cm^{-2} s^{-1}), along with the extinction constant employed, $c(\mathrm{H}\beta)$. Blank spaxels: three in the second row from top (broken Argus fibres); two per corner (fibres reserved for sky subtraction). The top two rows have not been considered in the physical analysis – see the text for details. The central star position is at coordinates (6, 15). North is up and east is to the right-hand side (cf. Fig. 1).

as Hβ. The He II λ4686 peak does not coincide with the Hβ-bright region but lies interior to it, by 2 spaxels, towards the inner nebula where the plasma ionization state is higher – there is also a local He II enhancement near the PN nucleus. The [Ne III] and [O III] maps are very similar and the lines peak at the same spots. The C II and O II ORL maps are also very similar and show peaks near the Hβ maximum, but also local peaks in the vicinity of the central star. Spaxels (3–5, 22) for the brightest emission lines of this PN appear with higher values than the mean, and may suffer to some unspecified degree from the same problem as row $Y = 22$ of NGC 5882. At the same time, the inset of Fig. 2 shows that there is a local flux enhancement within that IFU area.

4.1.3 NGC 7009

In Fig. 9, we present a similar set of maps for NGC 7009 as for NGC 6153. The Argus array targeted the northern part of the inner shell of the nebula and the long IFU axis lies in approximately the north-east to south-west direction (cf. Fig. 3). The most conspicuous feature in all maps is the bright arc that runs from top to bottom and shows high surface brightness spots at either end – this is mostly evident in light of Hβ but is also present in other wavelengths too. It can be safely identified with the rim of the inner bipolar nebular shell visible in the inset of Fig. 3. The rim appears fainter in the middle in all lines, except He II λ4686 and [Ar IV] λ4711 – the dust extinction

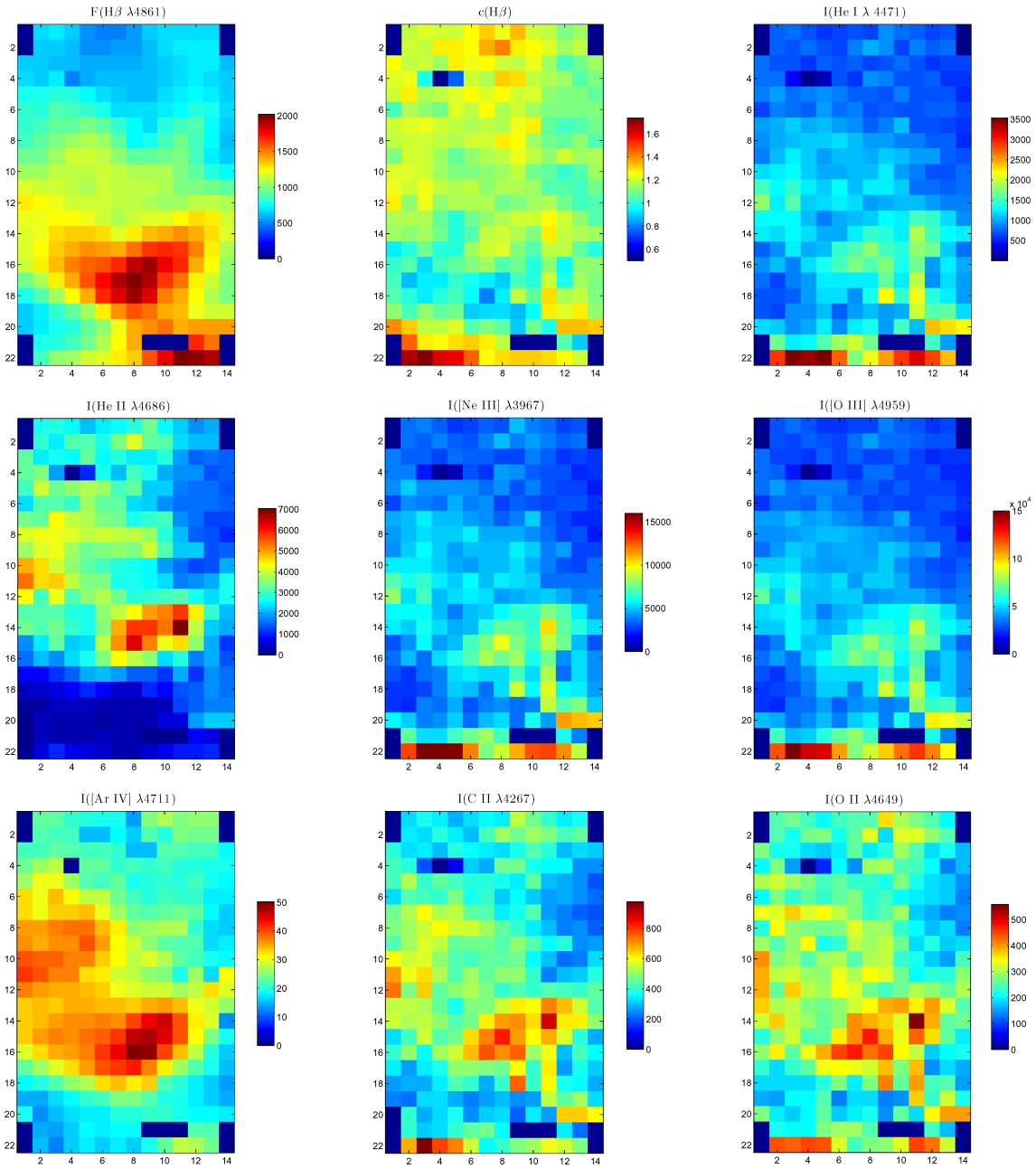

Figure 8. NGC 6153 monochromatic line flux (F) and dereddened intensity (I) maps (in units of 10^{-17} erg cm^{-2} s^{-1}), along with the extinction constant employed, $c(\mathrm{H}\beta)$. Blank spaxels: three in the second row from bottom (broken Argus fibres); two per corner (fibres reserved for sky subtraction). In this and subsequent figures, spaxels (3–5, 4) suffer from large uncertainties. The central star position is at coordinates (9, 3). North-west is up (cf. Fig. 2).

also drops there. The extinction constant displays some variability with a mean value of 0.183 ± 0.084 and an rms deviation of 0.111. The [Ar IV] line peaks at the lower segment of the rim, whereas He II shows high surface brightness spots in three positions along it. Characteristically, these spots are all shifted by 1 spaxel[4] towards the direction of the PN nucleus, relative to local enhancements of the Hβ emission, and should correspond to higher ionization zones perhaps associated with the star-facing side of an expanding shell, that is, zones that lie deeper in the nebula from the edge of the main ionization front. The C II λ4267 and O II λ4649 ORL maps have similar appearances and the lines also peak at the lower part of this nebular boundary.

[4] The seeing was less than 1.5 spaxels wide during these observations.

4.2 Plasma physical conditions

The dereddened emission-line maps discussed above were used to compute line ratio maps and hence the electron temperature (T_e) and density (N_e), and heavy ion abundances in the PNe relative to hydrogen. The nebular to auroral [O III] λ4959/λ4363 ratio was used to derive T_e, and the [Ar IV] λ4711/λ4740 ratio was used to derive N_e. Atomic data for [O III] and [Ar IV] were taken from Mendoza (1983) and Zeippen, Le Bourlot & Butler (1987), respectively. Mean values

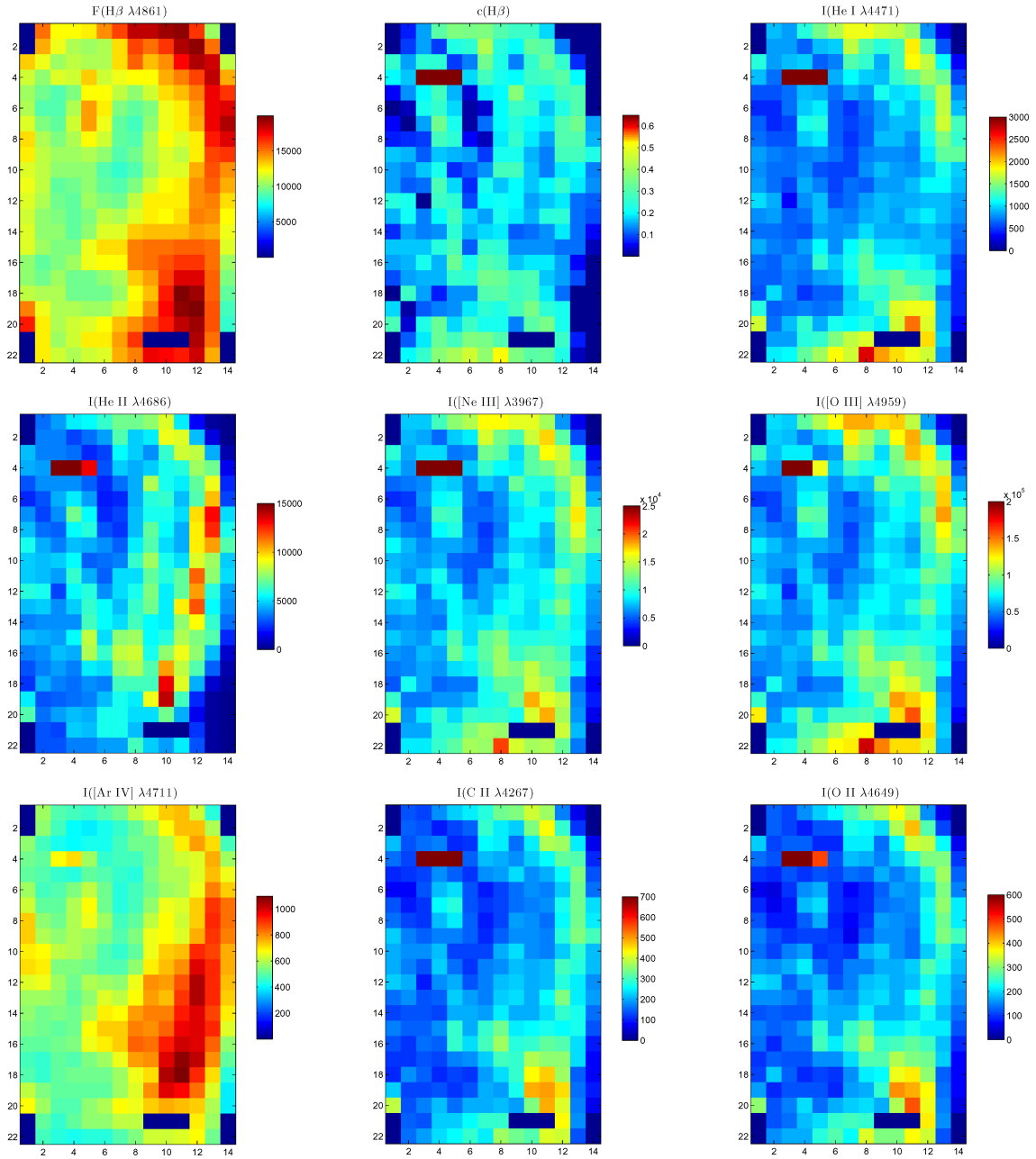

Figure 9. NGC 7009 monochromatic line flux (F) and dereddened intensity (I) maps (in units of 10^{-17} erg cm^{-2} s^{-1}), along with the extinction constant employed, c(Hβ). Blank spaxels: three in the second row from bottom (broken Argus fibres); two per corner (fibres reserved for sky subtraction). Spaxels (3–5, 4) typically suffer from large uncertainties. The central star position is at coordinates (3, 12). North-east is up (cf. Fig. 3).

of dereddened ratios of lines used in this study, and the corresponding plasma conditions for the PNe are reported in Table 2. These values are in very good agreement with results from the long-slit surveys.

Table 2 also tabulates the fractional mean-square temperature fluctuation parameters, t_A^2, and average electron temperatures, $T_{0,A}$, across the IFU area for each PN (that is, in the plane of the sky). We have used equations (11) and (12) of Mesa-Delgado, Esteban & García-Rojas (2007) for the derivation of these quantities (see also Rubin et al. 2002), based on the observed (T_e, N_e) spatial distributions. Very small values of the t_A^2 parameter in the plane of the sky are found in all three nebulae. The large uncertainties attached to (t_A^2, $T_{0,A}$) for NGC 6153 are dominated by the relatively large uncertainties in the per spaxel determination of N_e for this nebula. In the case of NGC 7009, our t_A^2 estimate of 0.00075 is about five times smaller than that derived by Rubin et al. (2002) from *HST*/WFPC2 imagery of the whole nebula in the [O III] lines. These results do not preclude the existence of large-scale temperature variations along a given line of sight. For instance, Barlow et al. (2006) have presented preliminary evidence for large line-of-sight T_e([O III]) variations in NGC 6153; however, as discussed in previous works, such large-scale temperature gradients cannot be the main cause of the abundance discrepancy problem (cf. Section 1). Furthermore, Barlow et al. (2006 and in preparation) discussed new

Table 2. Mean dereddened line ratios, physical conditions and fractional temperature fluctuation parameters. $F(\mathrm{H}\beta)$ are observed integrated fluxes across the IFUs. The line intensities are in units of $I(\mathrm{H}\beta) = 100$. See the text for details.

	NGC 5882	NGC 6153	NGC 7009
$c(\mathrm{H}\beta)$	0.45 ± 0.24^a	1.15 ± 0.12	0.18 ± 0.11
$F(\mathrm{H}\beta)$ (erg cm^{-2} s^{-1})	2.66×10^{-11}	3.12×10^{-12}	3.77×10^{-11}
I(He I λ4471)	5.47 ± 0.23	6.17 ± 0.34	4.90 ± 0.48
I(He II λ4686)	4.67 ± 3.27	17.4 ± 8.68	25.60 ± 8.27
I(C II λ4267)	0.491 ± 0.071	2.95 ± 0.58	1.04 ± 0.41
I(O II λ4089)	0.203 ± 0.108	0.679 ± 0.173	0.343 ± 0.098
I(O II λ4649)	0.433 ± 0.066	1.88 ± 0.41	0.882 ± 0.152
I([Ne III] λ3967)	30.09 ± 1.77	32.70 ± 1.68	44.15 ± 6.71
I([O III] λ4959)	342.3 ± 11.2	291.6 ± 14.2	372.3 ± 25.4
I([Ar IV] λ4711)	1.97 ± 0.33	2.66 ± 0.75	5.04 ± 0.88
[Ar IV] λ4711/λ4740	0.867 ± 0.085	0.972 ± 0.086	0.896 ± 0.034
[O III] λ4959/λ4363	250 ± 5	274 ± 47	187 ± 18
N_e (cm^{-3})	5160 ± 1200	3650 ± 1400	4780 ± 490
T_e (K)	9520 ± 190	9270 ± 410	$10\,340 \pm 380$
$T_{0,A}$ (K)	9560 ± 2260	9180 ± 11290	$10\,270 \pm 1970$
t_A^2	0.00034 ± 0.00021	0.00180 ± 0.00234	0.00075 ± 0.00016

[a]These are the uncertainties associated with the variation in the quantity across the IFU region (the rms deviation from the mean). They cannot be directly compared to the formal error on an integrated flux measurement for the same region: the uncertainties on the total integrated fluxes and ratios are >10 times smaller.

evidence that O II ORLs in NGC 6153 and NGC 7009 arise from cool plasma, based on their narrower line widths compared to that of the [O III] λ4363 line.

4.2.1 NGC 5882

In Fig. 10, maps for NGC 5882 of the dereddened [Ar IV] and [O III] diagnostic ratios are presented, along with their respective uncertainties determined from the line fitting (which incorporate the uncertainties derived from the pipeline processing), and the corresponding nebular N_e and T_e maps and their errors. The uncertainties on the [Ar IV] ratio are of the order of 10 per cent, whereas those on the [O III] ratio are typically smaller. The uncertainties on the N_e map are of the order of 10 per cent or less along the bright PN shell, but increase in lower surface brightness regions (towards the centre, and towards the south-east), where the [Ar IV] lines are weaker. The mean density is 5160 ± 465 cm^{-3} with an rms deviation of 1200 cm^{-3}. The T_e uncertainties are of the order of five per cent or less. The mean temperature is 9520 ± 50 K with an rms deviation of 190 K. The eastern part of the PN has the lowest (T_e, N_e). The observed range in temperature is ∼1000 K; a couple of local maxima are seen, the most conspicuous of which coincides with the Hβ-bright patch on the north-west part of the nebular shell. The mean electron temperature and density in the masked halo region, contained in the lower part of the IFU aperture [86 spaxels excluding (3–4, 4)], are somewhat lower than in the main shell, at 9380 ± 150 K and 2530 ± 600 cm^{-3}, respectively.

4.2.2 NGC 6153

The N_e and T_e maps of NGC 6153 (with the accompanying T_e uncertainties only) are presented in Fig. 11 (top panel). This PN shows a temperature range across the IFU of ∼1800 K, with a mean of 9270 ± 150 K and an rms deviation of 410 K. The demarcation line running diagonally across the error map is caused by the transition from single Gaussian profile fits to the [O III] λλ4363, 4959 lines (lower left) to double-peaked profiles (upper right). The errors are typically larger across the transition zone because of the increased uncertainty of fitting marginally resolved lines with double profiles. Where double Gaussian profiles were fitted, the combined flux of both was used in the analysis. The spectral resolution was high enough to allow a separate T_e determination for both nebular velocity components but, as the line S/N was not sufficiently high, this was not attempted.

There is a distinct negative temperature gradient from the nucleus towards the outer nebula (with increasing Y spaxel coordinates out to an offset of 10 arcsec from the nucleus; see also Fig. 15b). The highest values are observed near the nucleus, i.e. around spaxel (9, 3), but also in the neighbourhood of (2, 7). A T_e gradient of very similar magnitude along the minor axis of the PN was also observed by Liu et al. (2000), whose fixed long-slit position is contained within the IFU orientation (the IFU long-axis covers roughly half the extent over which those authors performed their spatial analysis). Our observations further resolve distinct local minima such as those at ∼(13, 8). Liu et al. concluded that the major part of the T_e gradient cannot be due to contamination of the λ4363 line from recombination excitation. In Sections 5.4 and 6, the temperature gradient is discussed in light of the inhomogeneous dust distribution and the higher dust extinction in the inner nebula.

From our analysis the N_e surface variation in NGC 6153 does not show a clear correlation with distance from the nucleus. The range in [Ar IV] density is ∼5000 cm^{-3} with a mean of 3650 ± 1520 cm^{-3} and an rms deviation of 1400 cm^{-3}. There is some evidence for slightly higher densities over the Hβ bright patch, and lower densities at spaxels beyond its outer edge [at ∼(3, 19); bottom left-hand IFU region). A similar rise in density was also seen by Liu et al. roughly correlating with Hβ surface brightness. No firm correlation between Hβ and N_e can be, however, established from the present analysis as the density uncertainties per spaxel are fairly high.

4.2.3 NGC 7009

This nebula shows a mean T_e of $10\,340 \pm 90$ K with an rms deviation of 380 K and a range across the IFU of 1700 K. In contrast to

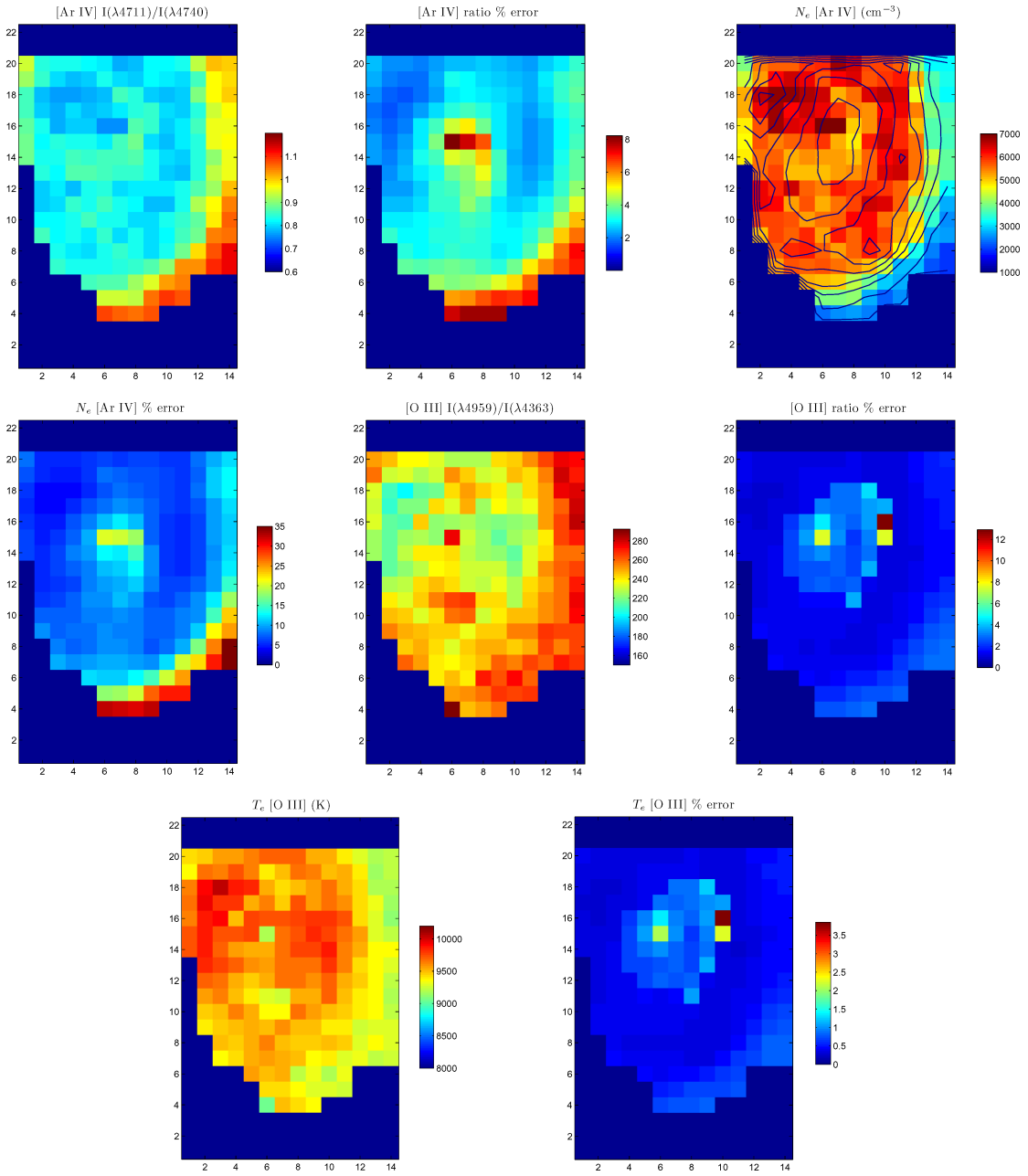

Figure 10. NGC 5882: maps of the dereddened [Ar IV] and [O III] line ratios and respective errors and of the derived electron density and temperature (and respective errors). The density map shows overplotted $F(\mathrm{H}\beta)$ isocontours.

NGC 6153, the temperature in NGC 7009 (Fig. 11, bottom) is not the highest close to the nucleus at map coordinates (3, 12), but at a position ∼5 arcsec north from it at (12, 13). That position coincides with the He II-bright high-excitation zone discussed in Section 4.1.3 (where the He^{2+}/He ionization fraction shows a local maximum; see also Fig. 14, bottom row), and marks the edge of the ionization front of the inner nebular bubble. The N_e surface variation across the IFU shows enhancements in the top and centre-bottom regions, approximately corresponding to local Hβ-bright spots; it is lower over spaxels (14, 13–20) where the Hβ surface brightness is low. The mean electron density across the IFU is 4780 ± 320 cm^{-3} with an rms deviation of 490 cm^{-3} and a range of ∼3000 cm^{-3}.

4.3 Chemical abundances

In this section, maps of the chemical abundances for the PNe are discussed. The O^{2+}/H^+ abundance ratio for all nebulae was derived from the [O III] λ4959 forbidden line, and also from the O II λ4089 3d–4f and λ4649 3s–3p ORLs. The C^{2+}/H^+ ratio was derived from the C II λ4267 ORL. The He^+/H^+ and He^{2+}/H^+ abundance ratios were derived from the He I λ4471 and He II λ4686 recombination lines, respectively; the sum of the two yielded total He/H abundance ratios for the three nebulae. The T_e([O III]) and N_e([Ar IV]) maps discussed above were adopted in all cases. The reader is referred to Tsamis et al. (2003, 2004) for details on the method of

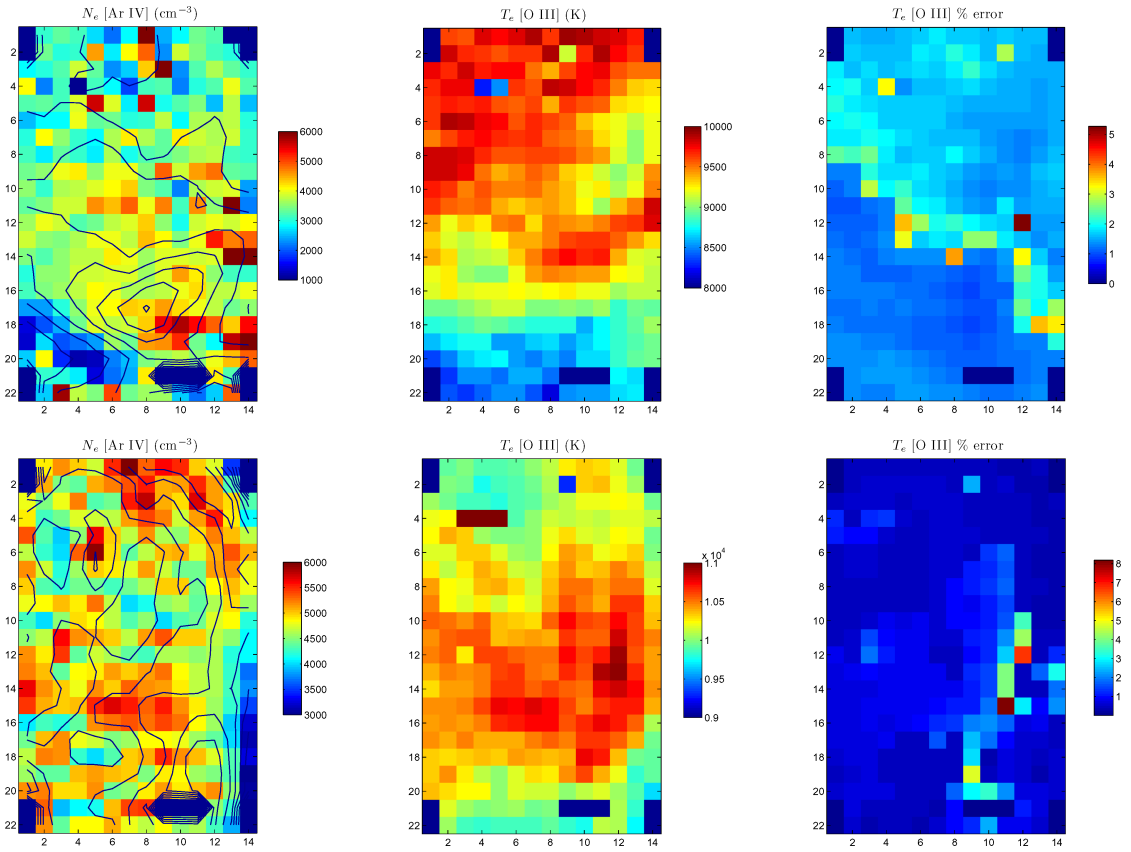

Figure 11. Electron density and temperature maps for NGC 6153 (top panel) and NGC 7009 (bottom panel). The density maps show overplotted $F(\mathrm{H}\beta)$ isocontours. Spaxels (3–5, 4) are not considered in the analysis.

calculating ionic abundance ratios based either on heavy element CELs or helium and heavier element ORLs. Effective recombination coefficients are taken from: Storey (1994) for O II λ4649; LSBC for O II λ4089; Davey, Storey & Kisielius (2000) for C II λ4267 (including both radiative and dielectronic processes); and Storey & Hummer (1995) for He I and He II. Table 3 summarizes the mean values from the maps presented in Figs 12–14, including the ADFs for O^{2+}. For all targets, the mean *ionic* C^{2+}/H^+ and O^{2+}/H^+ ORL abundance ratios are higher than the corresponding solar abundances of carbon and oxygen (e.g. Lodders 2003), by factors of ∼10 (NGC 6153), ∼3 (NGC 7009), and ∼2 (NGC 5882). We posit that these overabundance factors point towards the presence of heavy element-rich (hydrogen-poor) regions within the nebulae. The total carbon and oxygen recombination-line abundances, relative to hydrogen, for these regions should be even higher. The He/H abundances are also higher than solar for all PNe (by up to 40 per cent in the case of NGC 6153). In the presented maps, the posited hydrogen-deficient zones are identified as undulations in the ORL-based diagnostics.

4.3.1 NGC 5882

Abundance maps for NGC 5882 are presented in Fig. 12; the corresponding error maps are shown for the oxygen diagnostics. The O^{2+}/H^+ ratio based on the [O III] λ4959 CEL has a mean value of $(4.28 \pm 0.02) \times 10^{-4}$ with an rms deviation of 2.97×10^{-5}. The

Table 3. Mean chemical abundances and oxygen ADFs (the ratio of O^{2+} ORL over CEL determinations). The listed uncertainties are the formal errors on the mean. The rms deviations from the mean (associated with the variation in the quantity across the IFU region) are quoted in the text.

		NGC 5882	NGC 6153	NGC 7009
O^{2+}/H^+	[O III] λ4959	$(4.28 \pm 0.02) \times 10^{-4}$	$(4.09 \pm 0.26) \times 10^{-4}$	$(3.54 \pm 0.03) \times 10^{-4}$
O^{2+}/H^+	O II λ4089	$(1.83 \pm 0.21) \times 10^{-3}$	$(6.12 \pm 0.63) \times 10^{-3}$	$(3.12 \pm 0.25) \times 10^{-3}$
ADF(O^{2+})	λ4089/λ4959	4.33 ± 0.49	16.1 ± 2.0	9.10 ± 0.74
O^{2+}/H^+	O II λ4649	$(9.10 \pm 1.60) \times 10^{-4}$	$(4.17 \pm 0.61) \times 10^{-3}$	$(1.78 \pm 0.13) \times 10^{-3}$
ADF(O^{2+})	λ4649/λ4959	2.14 ± 0.35	10.9 ± 2.3	5.14 ± 0.35
C^{2+}/H^+	C II λ4267	$(4.68 \pm 0.37) \times 10^{-4}$	$(2.81 \pm 0.17) \times 10^{-3}$	$(1.01 \pm 0.05) \times 10^{-3}$
He^+/H	He I λ4471	0.1042 ± 0.0023	0.1182 ± 0.0062	0.0950 ± 0.0040
He^{2+}/H	He II λ4686	0.0039 ± 0.0001	0.0142 ± 0.0010	0.0213 ± 0.0003
He/H	$(He^+ + He^{2+})/H$	0.1081 ± 0.0023	0.1324 ± 0.0063	0.1163 ± 0.0040

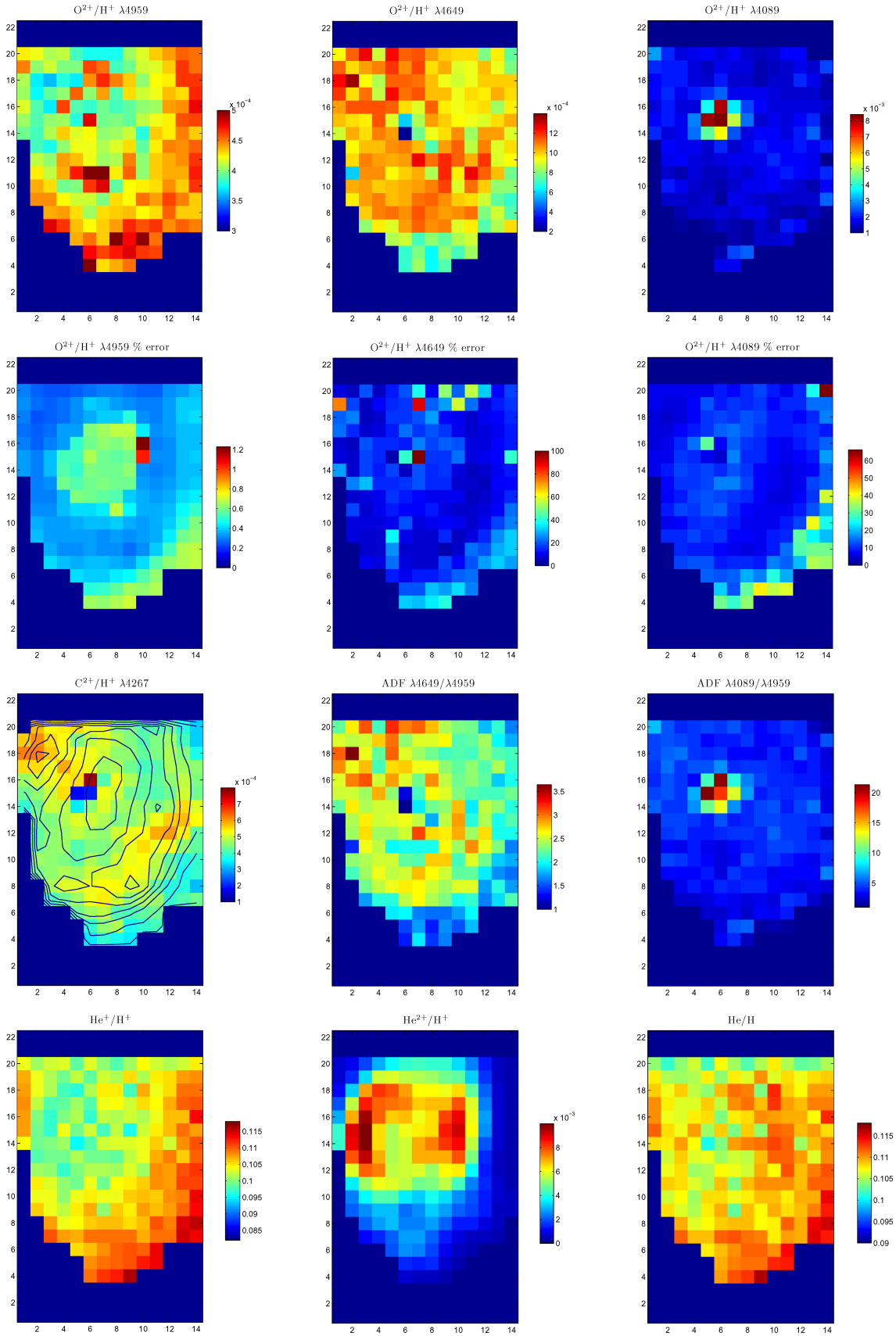

Figure 12. NGC 5882: O^{2+}/H^{+} abundance ratios from [O III] forbidden and O II recombination lines, C^{2+}/H^{+} abundances from the C II λ4267 ORL [with $F(H\beta)$ isocontours overplotted], the corresponding oxygen ADFs, and ionic and total He/H abundances from the helium ORLs.

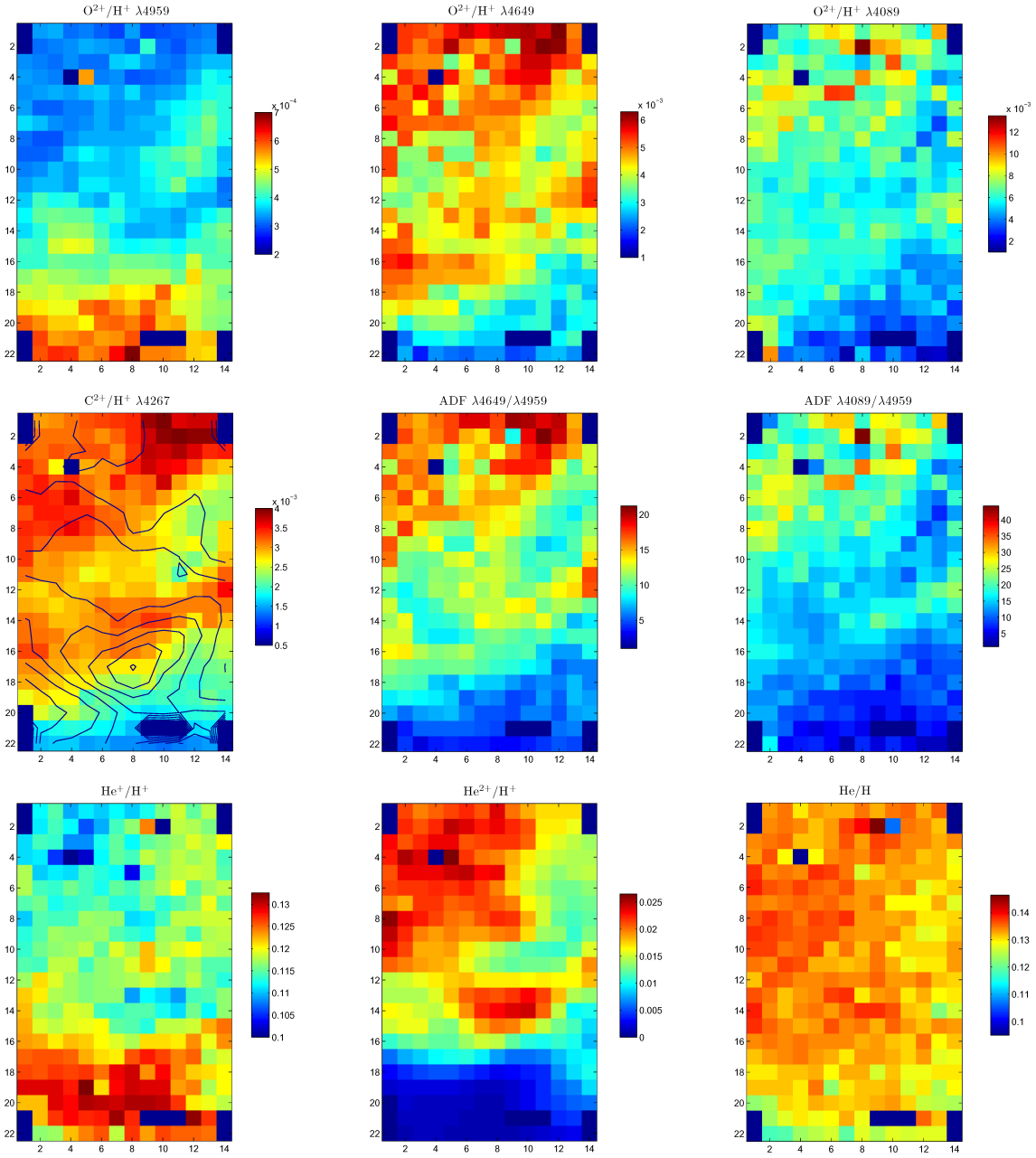

Figure 13. NGC 6153: O^{2+}/H^+ abundance ratios from [O III] forbidden and O II recombination lines, C^{2+}/H^+ abundances from the C II λ4267 ORL [with $F(H\beta)$ isocontours overplotted], the corresponding oxygen ADFs, and ionic and total He/H abundances from the helium ORLs. Spaxels (3–5, 4) are not considered in the analysis.

abundance of this ion shows a local maximum at the position of the PN nucleus at map coordinates (6, 15), surrounded by a ∼19 arcsec^2 area where the abundance is depressed, and two further maxima at positions symmetrically offset by ∼2 arcsec from the nucleus in the north–south direction. The CEL abundance of this ion is further depressed over the bright nebular shell but increases over the mean value on the eastern side of the PN, where the Hβ surface brightness and T_e([O III]) are low. In the masked halo region, the O^{2+}/H^+ CEL ratio is $(4.52 \pm 0.28) \times 10^{-4}$.

The O^{2+}/H^+ abundance ratio based on the O II λ4649 3s–3p ORL shows a mean of $(9.10 \pm 1.60) \times 10^{-4}$ with an rms variation of 1.22×10^{-4}. The lowest values of the ratio are found in the south-east corner of the IFU. The ionic abundance based on this line is perhaps slightly depressed over a 4 spaxel area in the vicinity of the nucleus with a value of $(6.00 \pm 3.13) \times 10^{-4}$. On the other hand, the O^{2+}/H^+ ratio based on the O II λ4089 3d–4f line shows a very different surface distribution relative to the λ4649 transition. Whereas the mean value is $(1.83 \pm 0.21) \times 10^{-3}$ with an rms deviation of 9.76×10^{-4}, the region in the vicinity of the PN nucleus over a 9 spaxel area shows a three times higher abundance with a value of $(5.52 \pm 0.61) \times 10^{-3}$. From the long-slit surveys, it was established that, on average, the λ4089 transition typically returns higher O^{2+}/H^+ ratios than the λ4649 transition when both line emissivities are calculated under the assumption of T_e([O III]) for their emitting regions. This effect, when attributed to the different T_e dependence of the emissivities of the two classes of O II transitions (3s–3p *versus* 3d–4f), has been

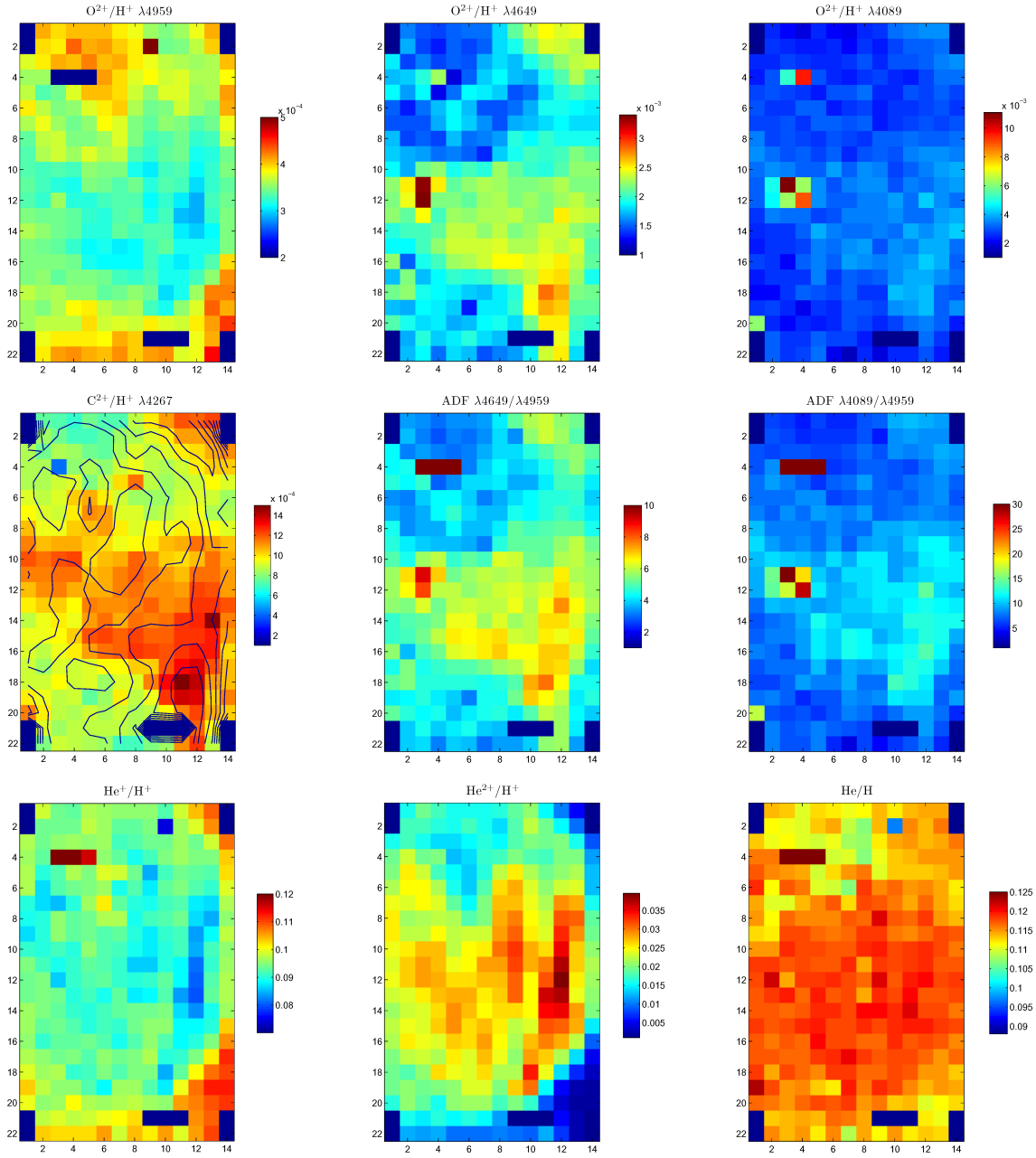

Figure 14. NGC 7009: O^{2+}/H^{+} abundance ratios from [O III] forbidden and O II recombination lines, C^{2+}/H^{+} abundances from the C II λ4267 ORL [with $F(H\beta)$ isocontours overplotted], the corresponding oxygen ADFs, and ionic and total He/H abundances from the helium ORLs. Spaxels (3–5, 4) are not considered in the analysis.

used to provide evidence for the existence of cold plasma regions in several PNe consistent with the existence of hydrogen-deficient regions (Tsamis et al. 2004; Liu et al. 2004). In Tsamis et al. (in preparation), we will revisit this issue and present a detailed analysis of the O II λ4089/λ4649 ratios from the present data set based on the latest effective recombination coefficients. In the masked halo region, the O^{2+}/H^{+} ORL ratio from the λ4649 and λ4089 lines is $(6.96 \pm 1.21) \times 10^{-4}$ and $(1.37 \pm 0.49) \times 10^{-3}$, respectively, rather consistent with the values across the main shell of the nebula.

We also present the respective O^{2+} ADF maps, that is the O^{2+} λ4649/O^{2+} λ4959 and O^{2+} λ4089/O^{2+} λ4959 quantities. These appear different (caused by the different behaviour of the O^{2+} ORL maps discussed above) with the former showing local maxima along the nebular shell and the latter showing a sharp maximum near the PN nucleus.

The C^{2+}/H^{+} ratio derived from the C II λ4267 ORL shows a mean of $(4.68 \pm 0.37) \times 10^{-4}$ with an rms deviation of 6.82×10^{-5}. Higher values are observed at the north-west and south-east segments of the Hβ-bright shell. The value of the ratio over 4 spaxels in the vicinity of the central star is $(4.26 \pm 1.11) \times 10^{-4}$ and is therefore consistent with the mean across the IFU (the strong stellar continuum in the neighbourhood of the PN nucleus can sometimes introduce higher errors in the line fitting – higher spectral resolution data would help in such cases). In the masked halo region, this abundance ratio is $(3.88 \pm 0.42) \times 10^{-4}$.

Finally, Fig. 12 (bottom panel) shows the helium abundance maps of NGC 5882. The mean He/H ratio is 0.1081 ± 0.0023 with an rms deviation of 0.0029. The He^+/H^+ abundance ratio is depressed in the central and western nebular regions, but is enhanced in the south and eastern area which is bordering on the PN halo. In contrast, the He^{2+}/H^+ abundance ratio shows two prominent maxima offset symmetrically on either side of the PN nucleus along the east-west axis. The He^+/H^+ ratio is inversely correlated with the He^{2+}/H^+ ratio across the IFU region (see Table A1). In the masked halo region, the He^+/H^+ and He^{2+}/H^+ ratios are 0.1142 ± 0.0056 and $(9.14 \pm 6.10) \times 10^{-4}$, respectively.

4.3.2 NGC 6153

Abundance maps for NGC 6153 are presented in Fig. 13. The O^{2+}/H^+ ratio based on the [O III] λ4959 CEL has a mean value of $(4.09 \pm 0.26) \times 10^{-4}$ with an rms deviation of 8.51×10^{-5}. The forbidden line abundance of this ion shows an inverse correlation with T_e([O III]), being high where the plasma temperature is low (characteristically in the outer nebula mainly; see Section 5) and vice versa. In contrast, the O^{2+}/H^+ ratio based on the O II λλ4089, 4649 ORLs generally increases towards the inner nebula, being proportional to the I(O II)/I(Hβ) brightness ratio surface distribution. Both of the O II recombination line abundance diagnostics show local maxima in the vicinity of the PN nucleus, but as in the case of NGC 5882 (and for the same reasons), their respective maps have a different appearance. For this reason, the λ4089/λ4959 ADF map shows values as high as ∼40 and the λ4649/λ4959 ADF map values as high as ∼20 at spaxels near the PN nucleus.

In the same vein, the C^{2+}/H^+ ratio derived from the C II λ4267 ORL, with a mean of $(2.81 \pm 0.17) \times 10^{-3}$ and an rms deviation of 5.72×10^{-4}, strongly peaks near the PN nucleus as well. Characteristically, both the ionic carbon abundance and the ionic oxygen abundance (from the O II λ4649 line) peak in the neighbourhood of spaxel (10, 2) about 2 arcsec from the nucleus; the O^{2+}/H^+ ratio from λ4649 has a value of $(6.14 \pm 0.81) \times 10^{-3}$ over a 3 spaxel area when the mean over the IFU is $(4.17 \pm 0.61) \times 10^{-3}$; this represents a local enhancement of 47 per cent over the mean. Across the same region the C^{2+}/H^+ ORL abundance is $(3.92 \pm 0.27) \times 10^{-3}$, that is 40 per cent higher than the mean. It therefore seems that in the case of NGC 6153 the PN nucleus, either in itself or via its hard radiation field, is strongly implicated in the causes of the abundance discrepancy, and in the high abundances derived from oxygen and carbon ORLs. The peaking of the C II and O II abundance diagnostics in the central PN regions had also been inferred from the long-slit analysis (Liu et al. 2000).

In Fig. 13 (bottom panel), we show the helium abundance maps of NGC 6153. The mean He/H ratio is 0.1324 ± 0.0063 with an rms deviation of 0.0039. The He^+/H^+ abundance ratio is lower in the inner nebular regions (mid-top IFU area), but is enhanced over its mean value in the outer nebula. In contrast, the He^{2+}/H^+ ratio is higher in the inner PN (see also Section 5). As with NGC 5882, there is an inverse linear correlation between the He^+/H^+ and He^{2+}/H^+ ratios across all spaxels (see Table A1). The total He/H abundance possibly shows a small positive gradient towards the inner nebula (top-left IFU area).

4.3.3 NGC 7009

In Fig. 14, abundance maps for NGC 7009 are presented. The O^{2+}/H^+ ratio based on the [O III] λ4959 CEL has a mean value of $(3.54 \pm 0.03) \times 10^{-4}$ with an rms deviation of 4.42×10^{-5}. In this PN also, the forbidden-line abundance of the O^{2+} ion shows an inverse correlation with T_e([O III]), being high where the plasma temperature is low (see Section 5) and vice versa. The abundance is generally depressed over a triangular region in the middle of the IFU. In contrast, over the same area the O II and C II recombination line abundance diagnostics are enhanced. There are prominent maxima in the O^{2+}/H^+ ORL ratio in the vicinity of the PN nucleus near map coordinates (3, 12) where the ratio based on the λ4649 line has a value of $(3.36 \pm 0.62) \times 10^{-3}$ over a 2 spaxel area; this constitutes a local enhancement of 89 per cent over the corresponding mean across the map of $(1.78 \pm 0.13) \times 10^{-3}$. The respective ADF maps show peaks near the nucleus as well. The C^{2+}/H^+ ratio peaks close to the nucleus with a value of $(1.14 \pm 0.16) \times 10^{-3}$ over a 4 spaxel area, but also near the edge of the Hβ-bright rim, some 5 arcsec away from the central star; it has a value of $(1.49 \pm 0.04) \times 10^{-3}$ at coordinates (11, 18). Its mean value across the IFU is $(1.01 \pm 0.05) \times 10^{-3}$ with an rms deviation of 1.57×10^{-4}.

In Fig. 14 (bottom panel), the helium abundance maps of NGC 7009 are shown. The mean He/H ratio is 0.1324 ± 0.0063 with an rms deviation of 0.0039. The He^+/H^+ abundance ratio is generally low over the triangular area where the O^{2+} and C^{2+} ORL abundances are enhanced, whereas the He^{2+}/H^+ ratio is correspondingly high there, peaking near the rim of the inner nebular bubble. There is a strong linear inverse correlation between the He^+/H^+ and He^{2+}/H^+ ratios in this nebula too (see Table A1). The total He/H abundance shows slightly lower values in the top of the IFU map, but does not vary across the edge of the inner nebular bubble where the He^{2+}/He ionization fraction peaks.

5 CORRELATIONS

In this section, we investigate several correlations between physical properties of the PNe that can be established following this analysis. Evidence for a few of these existed from the long-slit surveys, whereas others are new. A unique feature of this study, however, is that the large number of data points (∼300) per PN allowed us to put all these on a firm footing for the first time. Moreover, the 2D aspect of this analysis is particularly revealing, and in the following paragraphs it shall be brought to the fore. We present results for each nebula individually so as to first highlight the differences and then address the similarities; NGC 6153 is examined first.

5.1 NGC 6153

The O^{2+} ADF and the [O III] electron temperature for this PN show a very distinct correlation with distance from the PN nucleus. We have taken the Argus maps of these physical quantities (Figs 11 and 13) and binned all non-zero value spaxels at equal radii outwards from the position of the central star (with a radial increment of 1 spaxel); in Figs 15(a) and (b) the result is shown. As the [O III] temperature rises from the outer to the inner regions of the PN from ∼8400 to 10 000 K, characteristically the oxygen ADF rises as well. The quantity plotted in Fig. 15(a) is the λ4649/λ4959 ADF (and is also used in Figs 16–18), but a linear correlation is obtained for the λ4089/λ4959 ADF as well.

Fig. 15(c) shows the relationship between the oxygen ADF and T_e([O III]) for the 296 spaxels with a measurement of these quantities. The solid line is an error-weighted least-squares fit to the data with a correlation coefficient (r) of 0.92. In Fig. 15(d), the inverse relationship between the O^{2+}/H^+ abundance ratio based on the [O III] λ4959 line and T_e([O III]) is shown; the correlation is very tight in

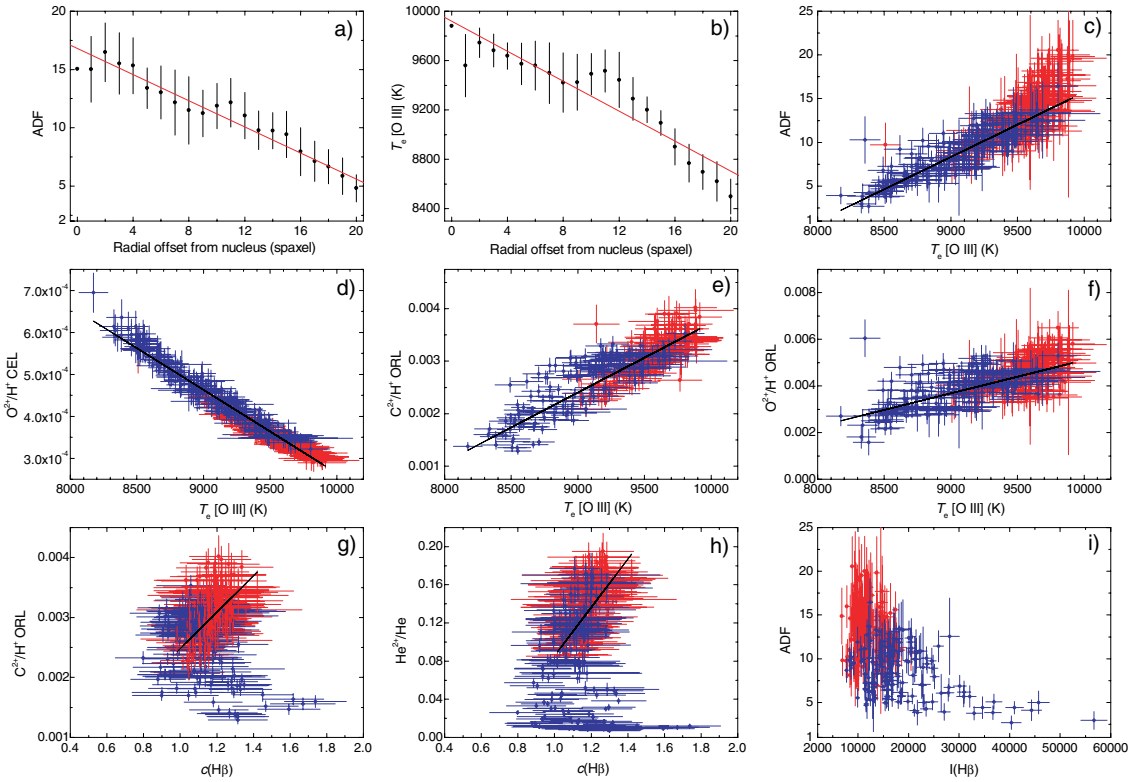

Figure 15. NGC 6153: correlations between various physical quantities: (a): the O^{2+} ADF and (b) the [O III] T_e radial profiles resulting from binning the respective Argus maps at equal radii from the central star. The full radial offset from the PN nucleus (20 spaxels) is 10.4 arcsec; (c)–(i): the red circles correspond to Argus IFU spaxel coordinates $(X, Y) = (1–14, 1–11)$ and the blue diamonds correspond to coordinates (1–14, 12–22) – see Fig. 8. The solid lines are weighted fits; (g)–(h): the solid lines are weighted fits to the red data points only. See the text for details.

this case too with a linear correlation coefficient of −0.98. In Figs 15 and 16, the black solid lines are least-squares fits weighted by the errors, the red circles denote data from spaxels with coordinates (from the corresponding Argus maps) of $(X, Y) = (1–14, 1–11)$, whereas the blue diamonds correspond to coordinates (1–14, 12–22). This colour scheme allows us to examine the behaviour of nebular properties in nebular regions that are near and far out from the central star (red and blue symbols, respectively; cf. also the orientation of the Argus IFU long axis viz. the position of the PN nucleus in Fig. 2). From the juxtaposition of Figs 15(a)–(b) and 15(c)–(d), a consistent picture emerges. Regions closer to the nucleus of NGC 6153 have higher temperature, lower forbidden line O^{2+}/H^+ abundance and exhibit higher O^{2+} ADFs than regions farther out in the nebula. Some unavoidable intermixing of the colour-coded data is seen due to projection (line-of-sight) effects and/or due to the fact that the steady progression from lower to higher temperatures has only been highlighted with a two-colour scheme.

In Figs 15(e)–(f), the correlations between the ORL abundance ratios C^{2+}/H^+ and O^{2+}/H^+ *versus* T_e([O III]) are plotted; the correlation coefficients of the error-weighted fits are in this case 0.88 and 0.70, respectively. These plots show that the recombination line abundances of doubly ionized carbon and oxygen, which are temperature-insensitive to a large degree, (i) rise towards the central nebular regions, and (ii) are typically the highest where the forbidden line [O III] temperature is highest. The O^{2+}/H^+ ORL ratio used in the correlations discussed and plotted in this section is based on the O II λ4649 line.

We also find a correlation of the C^{2+}/H^+ ORL abundance ratio and the He^{2+}/He ionization fraction *versus* the extinction constant, $c(H\beta)$; we performed least-squares fits for the inner nebula (∼148 data points) and show the results in Figs 15(g)–(h). Fig. 15(i) shows that an inverse trend is established between the oxygen ADF and the dereddened Hβ flux from each Argus spaxel. The trend is clearly non-linear. Regions of low surface brightness (in Hβ) that lie in the inner nebula exhibit the highest oxygen ADFs, whereas the low ADF 'tail' corresponds to brighter zones farther out in the nebula (most points in this tail correspond to spaxels of the last few IFU rows – large Y coordinates – on the far side from the PN nucleus).

The correlations between the ORL abundance ratios C^{2+}/H^+ and O^{2+}/H^+ *versus* the forbidden-line O^{2+}/H^+ abundance ratio are shown in Figs 16(a)–(b), where an inverse trend is seen in both cases with values of r of −0.86 and −0.69, respectively. These are mainly driven by the very strong linear correlation between the temperature-dependent forbidden-line O^{2+}/H^+ ratios and T_e([O III]) that was discussed earlier. In stark contrast, a positive correlation between the temperature-insensitive ORL C^{2+}/H^+ and ORL O^{2+}/H^+ abundance ratios is established with $r = 0.87$ (Fig. 16c). The fact that the trends between the ORL–CEL and ORL–ORL abundance diagnostics lie in completely opposite directions shows that (i) *vastly different assumptions govern the physical origins and the metallicity of the gas traced by ORL diagnostics on the one hand and CEL diagnostics on the other,* and that (ii) *consistent nebular metallicity estimates can in principle only be derived using pure ORL/ORL or CEL/CEL emission-line ratios*.[5] This further tells us that the C^{2+}/O^{2+} (pure ORL) abundance ratio is approximately constant throughout the

[5] This may not work for helium, however; see Section 6.

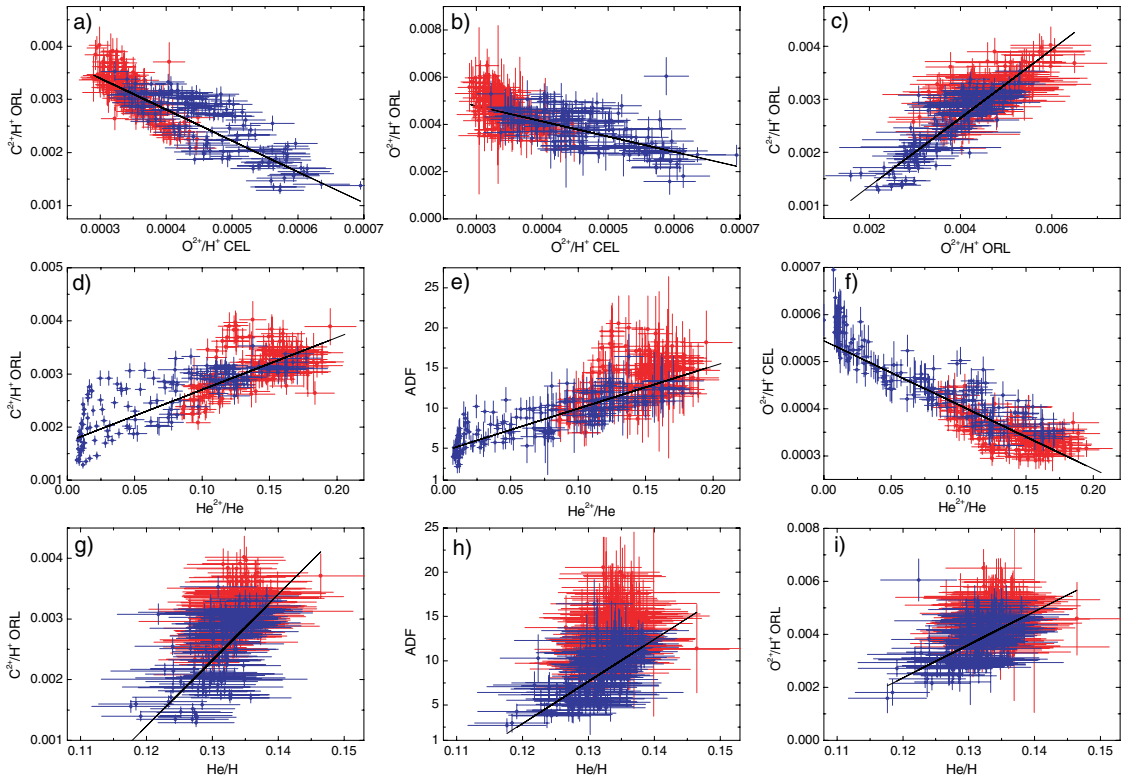

Figure 16. NGC 6153: correlations between various physical quantities with symbols as in Fig. 15; the solid lines are weighted fits. See the text for details.

portion of NGC 6153 observed in this programme with a mean value of 0.68 ± 0.11.

Figs 16(d)–(e) show that the C^{2+}/H^+ abundance ratio and the oxygen ADF are positively correlated with the He^{2+}/He ionization fraction with values of r of 0.85 and 0.86, respectively. The He^{2+}/He fraction rises close to the PN nucleus where the ionization degree of the nebular plasma is higher due to the harder radiation field, so these plots are again consistent with an origin for the ORL-emitting heavy element-rich plasma in the inner regions of the nebula. On the other hand, an inverse linear trend is established between the O^{2+}/H^+ CEL abundance ratio and He^{2+}/He ($r = -0.87$; Fig. 16f).

In Figs 16(g)–(i), the correlations between the C^{2+}/H^+ ORL abundance, the oxygen ADF, and the O^{2+}/H^+ ORL abundance *versus* the He/H abundance ratio are shown. Positive, but weaker, trends are seen in all cases with values of r of 0.68, 0.59 and 0.55, respectively. These plots also reveal that typically regions in the inner nebula show a somewhat higher helium abundance (but note that this large He/H is challenged in Section 6). Finally, we do not find any obvious trends of the C^{2+}/H^+ or O^{2+}/H^+ ORL abundances (or of the O^{2+} ADF) with electron density. The detailed parameters of our regression analysis for this nebula are listed in Table A1. Parameters of fits obtained when the O^{2+}/H^+ ORL abundance is based on the λ4089 line are also listed in Table A1 (the corresponding plots are not shown): the fits are all in the same direction as previously, and of similar strength, but with a slightly larger scatter [as the per spaxel uncertainties on $I(\lambda 4089)$ are somewhat higher].

5.2 NGC 7009

In this section, we examine whether the various correlations between diagnostics that were established for NGC 6153 hold for this nebula too. In order to check for any markedly different behaviour between nebular regions, the data from the Argus maps have been separated according to the following scheme: in the following plots, data from spaxels with coordinates – see Fig. 9 – $(X, Y) = (1–9, 5–19)$ are represented by the red circles, whereas data points outside this rectangular area are marked by the blue diamonds. The red symbols thus correspond to a nebular area of lower mean surface brightness (in dereddened Hβ) and of somewhat closer proximity to the PN nucleus than the blue symbols (cf. Fig. 3). The blue symbols comprise the zones of higher surface brightness and specifically the bright Hβ rim of the inner PN shell which runs from top to bottom in the Hβ image of the nebula (cf. Fig. 9 and the inset of Fig. 3 where this sharp boundary is clearly seen in the *HST* image). This nebula is, however, larger than NGC 6153 and the Argus IFU targeted the central regions of the inner bipolar shell; hence the adopted grouping of spaxels in the plots that follow may not be as clear-cut regarding their distance from the nucleus as it was for NGC 6153 where the IFU was both more favourably placed and captured a larger portion of the PN.

In Fig. 17(a), the inverse relationship between the O^{2+}/H^+ abundance ratio based on the [O III] λ4959 line and T_e([O III]) is plotted for the 296 spaxels with a measurement of these quantities. The solid line is an error-weighted least-squares fit to the data with a correlation coefficient of −0.94. The positive trend between the oxygen ADF and T_e([O III]) is shown in Fig. 17(b) and has a correlation coefficient of 0.78.

In Figs 17(c)–(d), the positive correlations between the ORL abundance ratios C^{2+}/H^+ and O^{2+}/H^+ *versus* T_e([O III]) are shown; the values of r of the error-weighted fits through the 135 red data points of the inner nebular field are in this case 0.66 and 0.70, respectively; they are 0.50 and 0.35, respectively, when fitting all the data.

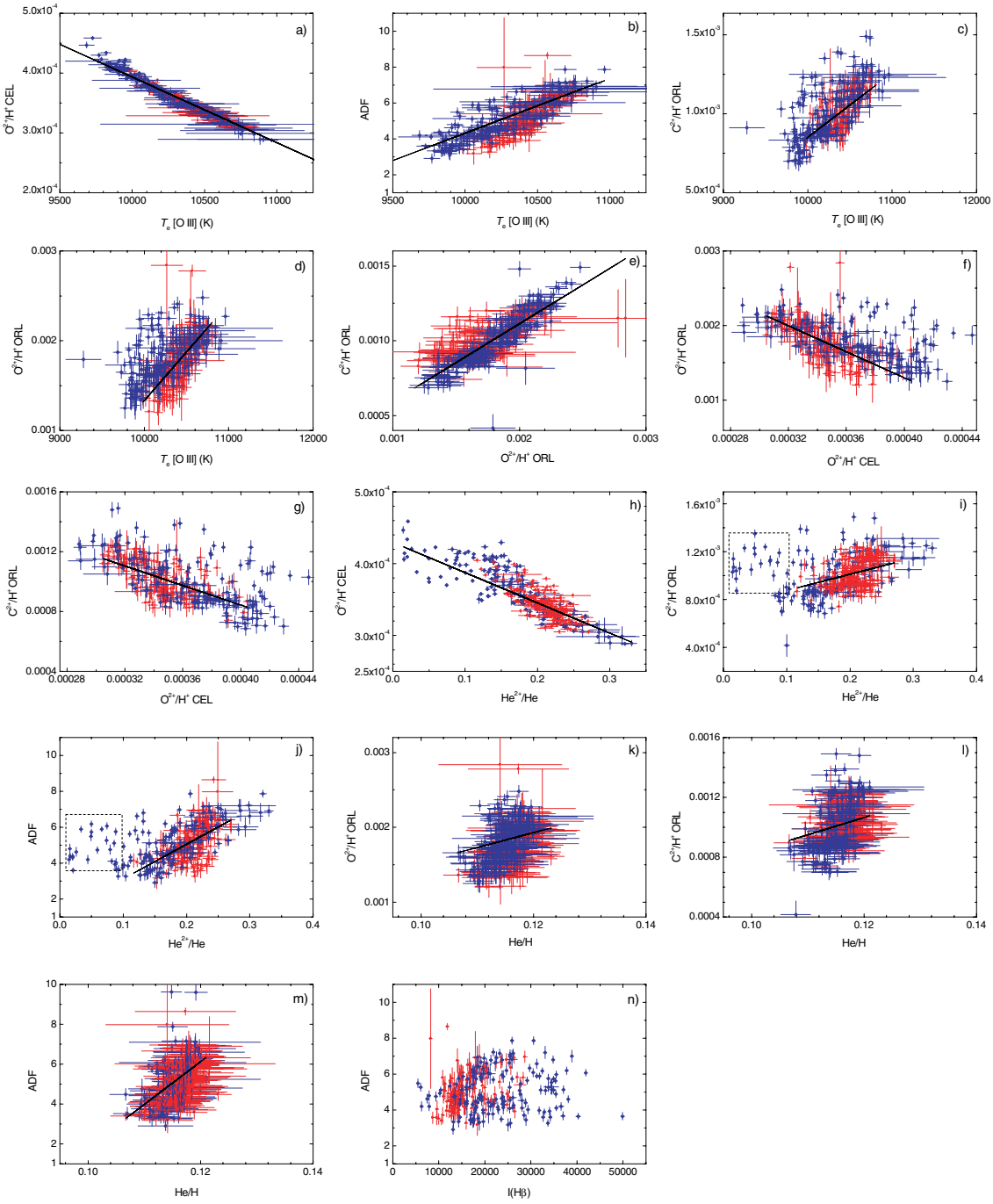

Figure 17. NGC 7009: correlations between various physical quantities. The solid lines are weighted fits. The red circles correspond to Argus IFU spaxel coordinates (X, Y) = (1–9, 5–19) and the blue diamonds correspond to spaxels outside this area (see Fig. 9); (f, g) and (i, j): the solid lines are fits to the red data points only. See the text for details.

These plots show that the recombination line abundances of doubly ionized carbon and oxygen for NGC 7009 follow the same trend with forbidden line temperature as was the case of NGC 6153. The O^{2+}/H^+ ORL ratio used in the correlations plotted in this section is based on the O II λ4649 line.

In Figs 17(f)–(g), we plot the correlations between the ORL abundance ratios O^{2+}/H^+ and C^{2+}/H^+ *versus* the forbidden-line O^{2+}/H^+ abundance ratio, where an inverse trend is seen in both cases with values of r of −0.68 and −0.63, respectively, for fits to the red data points. When fits to all data are performed, the coefficients are less than 0.50 due to the larger scatter of some of the blue data points which correspond to nebular zones of higher mean surface brightness. The general behaviour of the trends is the same as for NGC 6153. A positive correlation between the temperature-insensitive ORL C^{2+}/H^+ and ORL O^{2+}/H^+ abundance ratios is established ($r = 0.86$; Fig. 17e). The C^{2+}/O^{2+} (pure ORL) abundance

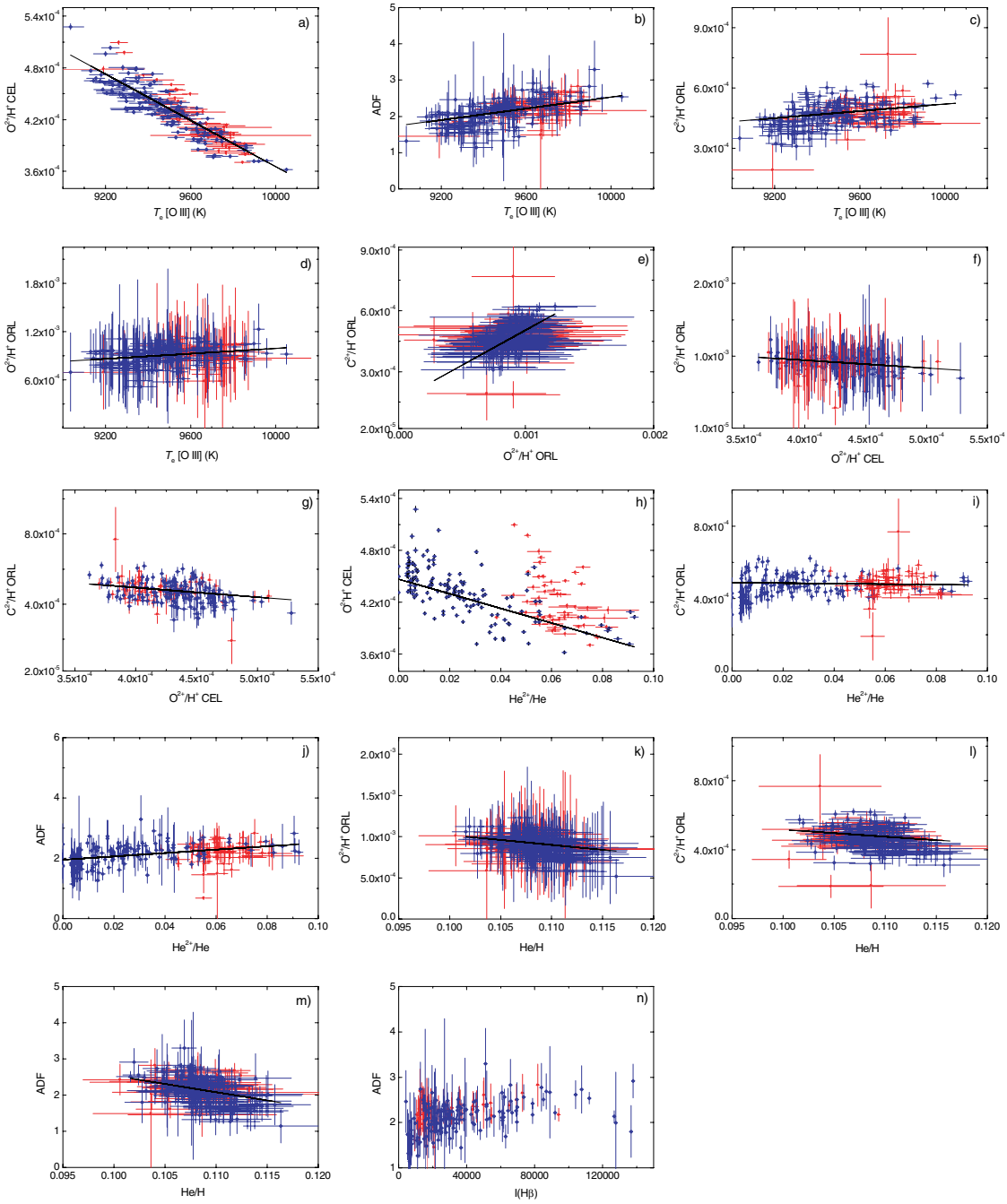

Figure 18. NGC 5882: correlations between various physical quantities. The red circles correspond to Argus IFU spaxel coordinates $(X, Y) = (4–10, 11–18)$ and the blue diamonds correspond to spaxels outside this area (see Fig. 7). The solid lines are linear fits weighted by the errors (only through the blue data points in panel 'h'). See the text for details.

ratio is approximately constant throughout the field but there are a few (red) points a factor of ∼1.27 higher (but within 2σ) than the mean ratio of 0.57 ± 0.05.

Figs 17(i)–(j) show that the C^{2+}/H^+ ORL abundance ratio and the O^{2+} ADF are positively correlated with the He^{2+}/He ionization fraction with values of r of 0.35 and 0.55, respectively (for fits through the red data points only). The O^{2+}/H^+ CEL ratios are inversely correlated with the helium ionization state (the weighted fit to all data has an r of −0.84). There is more scatter in these plots than was the case for NGC 6153: the cluster of low-ionization points within the dashed squares in Figs 17(i)–(j) (at ADF ∼5) come from the lower-right corner of the corresponding He^{2+}/He map and also from IFU row $Y = 14$; they are also of relatively high O^{2+}/H^+ (forbidden-line) abundance. The main trends identified in these plots are in the same vein as for NGC 6153, with high ionization gas exhibiting higher oxygen ADFs and higher C^{2+}/H^+ ORL abundance ratios than lower ionization, high O^{2+}/H^+ CEL regions.

Figs 17(k)–(m) show the ORL O^{2+}/H^+ and C^{2+}/H^+ abundance ratios and the O^{2+} ADF *versus* the He/H abundance ratio. Weak positive trends are seen in all cases – for the O^{2+} ADF versus He/H linear fit, $r = 0.58$. The trends are in the same direction as in the case of NGC 6153. We further plot the O^{2+} ADF *versus* the dereddened

Hβ intensity per spaxel in Fig. 17(n). No clear trend is seen in contrast to the NGC 6153 case. We do not find any obvious trends of the C^{2+}/H^+ or O^{2+}/H^+ ORL abundances (or of the O^{2+} ADF) with electron density. No firm trend of the heavy element ORL abundances with the extinction constant is found in contrast to the case of NGC 6153. The detailed parameters of our regression analysis for this nebula are listed in Table A1. Parameters of fits obtained when the O^{2+}/H^+ ORL abundance is based on the λ4089 line are also listed in Table A1 (the corresponding plots are not shown): the fits are in the same direction as previously.

5.3 NGC 5882

This PN is the smallest of the three and its symmetrical inner shell was almost fully captured by the Argus IFU. It also displays lower mean oxygen ADFs and was meant to be our 'control' target. In this section, we explore correlations between the same set of quantities for NGC 5882 as for the other two nebulae. The Argus spaxels were grouped based on their distance from the nucleus in the following manner (cf. Fig. 7): points with spaxel coordinates $(X, Y) = (4–10,11–18)$ are coded as red circles whereas those exterior to this boxed region are coded as blue diamonds.

Fig. 18(a) shows the O^{2+}/H^+ abundance ratio based on the [O III] λ4959 line *versus* T_e([O III]) for the 203 spaxels with a measurement of these quantities (that is, excluding the masked halo region of the nebula). The solid line is an error-weighted least-squares fit to the data with a correlation coefficient of -0.89. The positive trend between the oxygen ADF and T_e([O III]) (Fig. 18b; $r = 0.52$) is not as strong as for the other two PNe. In Figs 18(c)–(d), we plot the C^{2+}/H^+ and O^{2+}/H^+ ORL abundance ratios *versus* T_e([O III]); both show loose positive trends (with equal $r = 0.27$). The O^{2+}/H^+ ORL ratio used in the correlations plotted in this section is based on the O II λ4649 line.

The O^{2+}/H^+ and C^{2+}/H^+ ORL abundances are plotted against the forbidden-line O^{2+}/H^+ abundance ratio in Figs 18(f)–(g); loose negative trends are established in both cases, but in the same vein as for NGC 6153 and NGC 7009 where the trends were stronger. The C^{2+}/H^+ ORL abundance is positively correlated with the O^{2+}/H^+ ORL abundance ratio ($r = 0.61$; Fig. 18e) following the same trend as for the other targets. The C^{2+}/O^{2+} (pure ORL) abundance ratio of NGC 5882 is approximately constant across the IFU region with a mean value of 0.52 ± 0.11.

A loose negative trend is seen between the O^{2+}/H^+ CEL abundance and the He^{2+} ionization fraction (mostly for low-ionization gas represented by the blue data points with $r = -0.68$; Fig. 18h). The C^{2+}/H^+ ORL abundance shows a flat trend with increasing He^{2+}/He (Fig. 18i), in contrast to the cases of NGC 6153 and NGC 7009, while the O^{2+} ADF shows a week positive correlation with He^{2+}/He (Fig. 18j; $r = 0.42$). The excitation state of the gas in this PN is, however, the lowest of the three, with less than 10 per cent of helium being doubly ionized (compared with values of up to 20 and 30 per cent for NGC 6153 and NGC 7009, respectively).

No clear trends are seen between the doubly ionized carbon and oxygen ORL abundances, and the O^{2+} ADF *versus* the total He/H abundance (Figs 18k–m) when positive trends were established for the other two nebulae. Finally, no trend is established between the O^{2+} ADF and the Hβ intensity per spaxel either (Fig. 18n). The trend between the C^{2+}/H^+ ORL abundance ratio and the extinction constant is flat and is not shown (parameters of the fit are, however, listed in Table A1). Detailed parameters of our regression analysis of NGC 5882 are listed in Table A1, including those obtained when the O^{2+}/H^+ ORL abundance is based on the λ4089 line; those fits are in the same vein as previously.

5.4 Correlations: what do they tell us?

A strong inverse correlation between the CEL-based O^{2+}/H^+ abundances and T_e([O III]) is established for all three sources. The O^{2+}/H^+ CEL abundance decreases by factors of approximately 2.0, 1.5 and 1.3 over values of ΔT_e of $\sim +1600$, $+1100$ and $+700$ K in NGC 6153, NGC 7009 and NGC 5882, respectively (Figs 15d, 17a and 18a). The exponential dependence of CEL-based abundances on the adopted electron temperature (the Boltzmann factor) mathematically suppresses most of the scatter in O^{2+}/H^+ induced by errors in the T_e([O III]) determination, thus strengthening the correlation. However, the correlation mostly reflects a physical process since the variation in temperature with position is not random (see NGC 6153, but also NGC 7009 where regions closer to the nucleus have a higher mean temperature), and T_e([O III]) shows a high degree of correlation with other essentially independent quantities such as the C^{2+}/H^+ and O^{2+}/H^+ ORL abundances. A physical correlation is expected as well, since [O III] is a dominant coolant of the gas: where the concentration of O^{2+} is lower, T_e([O III]) will tend to be higher. This may be due to a real variation in the O/H abundance or to a variation in the O^{2+}/O ionization fraction. Assuming a constant O/H, the higher forbidden-line temperature in the inner nebular regions can be qualitatively understood if part of the O^{2+} ionic component shifts into O^{3+}; this is a likely possibility since O^{3+} must coexist with He^{2+} (based on ionization stratification considerations), and the O^{2+}/H^+ CEL abundance inversely correlates with He^{2+}/He (Figs 16f, 17h and 18h).

Along the same lines, contrasting NGC 6153 with NGC 5882, the observed range of T_e([O III]) across the respective IFU regions is larger where the He^{2+} zone is more prominent (i.e. in the former rather than in the latter nebula). The large opacity of He^+ and the relatively large average energy of the corresponding photoelectrons both contribute to further heat the high-ionization region. That the inner nebula electron temperature can be explained in this way should await quantitative analysis by means of photoionization models tailored to these observations. Extra heating can be provided by the photoelectric effect on small dust grains that may populate the vicinity of the central stars (see Section 6). The variety of potential heat sources and the associated uncertainties can make potential spatial variations in O/H in the gas phase that emits [O III] λ4959 difficult to ascertain. One intriguing aspect is the fact that T_e([O III]) continues to decrease outwards in NGC 6153, even in regions where He^{2+} and O^{3+} should in principle be minor species. It may be that He^{2+} can survive relatively farther out from the nucleus than expected as the gas 'porosity' induced by density fluctuations can blur out the theoretical ion stratification.

The second fundamental piece of information from this analysis is the clear positive correlation of the C^{2+}/H^+ and O^{2+}/H^+ ORL abundances *versus* T_e([O III]) for all three targets – even for the low ADF 'control' NGC 5882. Throughout the IFU region of NGC 6153, for instance, these abundances increase by a factor of ~ 2 (Figs 15e–f) from the outer to the inner nebula, so that the corresponding increase in the O^{2+} ADF is a factor of ~ 4 (Fig. 15c). This is paradoxical in that ORLs should a priori be enhanced in low-T_e conditions (due to their emissivities obeying an inverse power law with electron temperature). If a sizeable fraction of the (optical) [O III] flux were to arise from the same parcel of gas emitting a sizeable fraction of ORL flux, then part of the [O III] emission would necessarily be produced at relatively low electron temperatures and the

(observed) average T_e([O III]) would be lower (*not higher*), where ORL emission is strongest. *Thus, this paradox demonstrates beyond reasonable doubt that heavy element CELs and ORLs must essentially arise from unrelated gas components.*

The 'dual abundance' picture of two distinct components of highly ionized gas at very different temperatures can solve the paradox, but the only known way to maintain a strongly photoionized gas at low T_e is thermostasis by fine-structure (FS) IR lines. This mechanism can only be effective for sufficiently large heavy-element abundances (and sufficiently low electron densities so that the low critical density FS lines are not quenched). This interpretation of the data is qualitatively coherent since cool hydrogen-deficient ionized gas propitiously emits ORLs. Therefore, at another quantitative level (separate from ORLs), an essential check can be provided by the 2D spatial distribution of IR FS line emission; this should be tractable by means of *Spitzer Space Telescope* observations and future *Herschel* surveys.

6 DISCUSSION AND CONCLUSIONS

We have presented the first detailed analysis of IFU spectrophotometry of three Galactic PNe (NGC 5882, NGC 6153 and NGC 7009) taken with the 8.2-m VLT and demonstrated the superb capability of FLAMES Argus data for the accurate mapping of the physical properties of nebulae. Spatially resolved maps of 11.5×7.2-arcsec^2 areas of the PNe with 0.52^2 arcsec^2 spaxels were made in the light of [O III] λ4959 and [Ne III] λ3967 lines, and the Hβ λ4861, He I λ4471, He II λ4686, C II λ4267, O II λ4089 and λ4649 recombination lines. The dust extinction and the plasma temperature and density were mapped out, along with the ionic abundances of helium, C^{2+}, and O^{2+}, relative to hydrogen. The O^{2+}/H^+ ratio was derived from the O II ORLs and the [O III] λ4959 CEL. Maps of the resulting O^{2+} ADF were made. The O^{2+} ADF varies between the targets and across the Argus field of view in each case. In NGC 6153 and NGC 7009, the O^{2+} ADF and the C^{2+} ORL abundance show distinct spikes at or near the nucleus. In NGC 7009, these quantities further peak at positions coinciding with the high-excitation boundary between the inner nebular shell and the outer envelope; this feature is well registered on both the Argus maps and the *HST* WFPC2 image. In NGC 5882, where the S/N of O II ORLs is lower, the O^{2+} ADF derived from the λ4089/λ4959 diagnostics also peaks at the position of the central star.

In all cases, these local maxima are observed over about 2 spaxels (∼1 arcsec) and are therefore at the limit of our spatial resolution. This means that the hypothetical structures associated with the hydrogen-poor plasma should have physical dimensions of <1000 astronomical units (au), assuming a typical PN distance of the order of 1 kpc.

Correlations between the O^{2+} ADF and the ionization state of the gas as gauged by the He^{2+}/He ionization fraction were established for NGC 6153 and NGC 7009; likewise strong correlations of the O^{2+} ADF and the C^{2+}/H^+ and O^{2+}/H^+ ORL abundances *versus* the forbidden line electron temperature were established for these nebulae (for NGC 5882 these correlations were weaker but in the same direction). This constitutes new evidence that the 'metallic' ORLs in these PNe are somehow associated with highly ionized plasma, and that heavy element ORLs and CELs arise from largely unrelated parcels of gas, in accordance with dual-abundance photoionization models (Péquignot et al. 2002). We argue that this hydrogen-deficient, highly ionized plasma may well (i) have been recently ejected from the nucleus in the form of clumped gas, or (ii) be part of circumstellar material very close to the star in the form of a disc-torus structure (based on the spatial correlation of the diagnostics with the position of the central star), or equally that (iii) it originates from high-excitation gas presently being photoevaporated from milliparsec scale neutral condensations embedded in the nebulae at the limit of our spatial resolution.

In case (i), *the physical origin of the enhanced heavy-element ORL emission could be an ensemble of hydrogen-poor clumps analogous to the H-poor knots observed in the class of nebulae, such as Abell 30 or Abell 58* (e.g. Borkowski et al. 1993; Guerrero & Manchado 1996), which may have undergone a late helium-flash (Iben et al. 1983) or could be associated with neon novae (Wesson et al. 2008). In this context, the range of ADFs found amongst our targets could reflect an evolutionary effect with H-poor zones becoming progressively more readily observed as the density and temperature contrast between them and the ambient expanding nebula increases over time. One should recall that NGC 5882 is positioned in the lower end of the 'ADF sequence' established from the long-slit surveys according to which dense, compact and lower ionization PNe exhibit smaller integrated abundance discrepancies than more diffuse, larger and higher ionization nebulae. NGC 6153 and NGC 7009, on the other hand, appear to be in a more advanced stage of the 'ADF evolution' (Liu et al. 2004; Tsamis et al. 2004).

In case (ii), *the hydrogen-deficient gas could arise from circumstellar structures* such as those recently discovered by VLT interferometric observations in association with J-type C-stars (IRAS 18006−3213 – Deroo et al. 2007a), post-asymptotic giant branch stars (V390 Vel – Deroo et al. 2007b) and PNe (Mz 3 – Chesneau et al. 2007). These toroidal structures have estimated radii of <1000 au and there is evidence that they contain large amounts of silicate dust. The inference about their chemistry is important as the C/O ORL abundance ratio derived for our PN sample is lower than unity; this means that an association of the hydrogen-poor, O-rich gas with silicate-based (i.e. oxygen-rich) dust is not unlikely (see below).

In case (iii), *the H-poor plasma could originate in evaporating dusty 'cometary knots' analogous to those in the Helix nebula* (NGC 7293; e.g. Meaburn et al. 1992) immersed in high ionization nebular zones both near (NGC 5882, NGC 6153, NGC 7009) and farther out (NGC 7009) from the stars. The Helix globules, however, are rich in molecular hydrogen (Meixner et al. 2005) and this hypothesis would require a mechanism for the efficient removal of hydrogen and/or the chemical differentiation of the evaporated gas for the spectroscopic signature of H-poor plasma to be observed. Also, in the Helix nebula at least, there is no evidence of globules inside the high ionization He II zone or of He II emission from the observed globules, and these features are mostly associated with emission from lower ionization species (O'Dell et al. 2002; O'Dell, Henney & Ferland 2007); in contrast, as we have shown, the H-poor plasma in our PNe is associated with He II emission. On the other hand, this *does not* preclude that 'molecular' globules can be effectively destroyed in the inner regions of PNe whilst leaving pockets of H-poor plasma behind. This hypothesis can clearly be put to the test with observations of the type presented in this work.

We have presented evidence that, in the central regions of NGC 6153, the C^{2+} ORL abundance, the He^{2+}/He ionization fraction and the O^{2+} ADF are weakly correlated with the extinction constant. There is marginal evidence that this may hold for the inner parts of NGC 7009 as well. This correlation, if real, could corroborate either the 'dusty clump evaporation' scenario or the 'dusty disc' scenario for the origin of the hydrogen-deficient gas. Dust-rich regions can contribute to the heating of their plasma environs via photoelectric gas heating (e.g. Dopita & Sutherland 2000; Stasińska & Szczerba 2001; Weingartner, Draine & Barr 2006) and to the metal

enrichment of the gas via grain destruction, thus bringing about this correlation. According to Dopita & Sutherland, dust grain photoelectric heating is more effective in regions with a population of small grains, it increases with increasing grain metallicity, and is more important in highly ionized regions. This effect could also play a role in the observed rise of T_e([O III]) in the inner NGC 6153 regions (in parallel to usual photoionization which can also enhance the electron temperature in the He^{2+} zone), although coupled dust/plasma models would be needed to ascertain and quantify this. Alternatively, since the theoretical Hγ/Hβ line ratio decreases with decreasing electron temperature (Storey & Hummer 1995), and since the extinction constant (based on Hγ/Hβ) was computed here adopting T_e([O III]), the positive correlation of c(Hβ) with the ADF may be indicative of the fact that H I lines in PNe partly arise from cool gas which emits most of the heavy element ORLs, in accordance with dual-abundance models.

Relatively weak correlations between the O^{2+} ADF and the O^{2+}/H^+, C^{2+}/H^+ ORL abundances *versus* the He/H ratio in NGC 6153 and (in the inner regions) of NGC 7009 have been established. This result, which should be backed up by further studies, constitutes new observational evidence that corroborates the predictions of the dual-abundance PN models of Péquignot et al. (2002, 2003). In those models, the heavy element-rich (H-poor) gas component, which is responsible for the bulk of the heavy element ORL emission, is also helium-rich and as such it contributes non-negligibly to the emissivity of the helium ORLs. When this effect is not accounted for, as in empirical methods like the one we have used in this work, there is an insidious bias towards overestimating the helium to hydrogen abundance ratio. Based on our results it is therefore clear that total He/H abundances of PNe as traditionally determined from empirical methods, and which assume chemical uniformity of the plasma, will be systematically overestimated. Again detailed modelling in the context of a chemically inhomogeneous nebula is needed to remove this bias. With respect to helium, it should be noted that, in contrast to He^{2+}, He^+ is not perturbed by H-poor material, since nebular regions with high He^{2+}/H^+ give the same (He^+ He^{2+})/H ratio as regions with low He^+/H^+.

In conclusion, our detailed IFS analysis of a few suitable objects has allowed us to identify important new elements of the still incomplete puzzle of PN astrophysics, and we have put forward testable proposals for the likely nature of some of the missing pieces. Furthermore, this study has underlined a number of clear requirements that a detailed solution to the 'ORL versus CEL' problem should meet, if it were to be successful.

ACKNOWLEDGMENTS

We thank A. Blecha and G. Simond of the Geneva Observatory for answering our queries on girBLDRS and for providing extra calibrations and patches. Marina Rejkuba is thanked for early advice on the reduction of Argus data. Francesca Primas is thanked for an informed explanation of the 'scattered light' issue mentioned in Section 3. We appreciate comments from Bob O'Dell and thank the referee for a constructive report. This study has made use of the NASA ADS data base. YGT gratefully acknowledges the hospitality of ESO Garching where part of this work was completed during a science visit.

REFERENCES

Allington-Smith J., 2006, New Astron. Rev., 50, 244
Barlow M. J., Hales A. S., Storey P. J., Liu X.-W., Tsamis Y. G., Aderin M. E., 2006, in Barlow M. J., Méndez R. H., eds, Proc. IAU Symp. 234, Planetary Nebulae in our Galaxy and Beyond. Cambridge Univ. Press, Cambridge, p. 367
Blecha A., Simond G., 2004, GIRRAFE BLDR Software Reference Manual 1.12 (http://girbldrs.sourceforge.net)
Borkowski K. J., Harrington J. P., Tsvetanov Z., Clegg R. E. S., 1993, ApJ, 415, L47
Chesneau O. et al., 2007, A&A, 473, L29
Corradi R. L. M., Gonçalves D. R., Villaver E., Mampaso A., Perinotto M., 2000, ApJ, 542, 861
Davey A. R., Storey P. J., Kisielius R., 2000, A&AS, 142, 85
Deroo P., van Winckel H., Verhoelst T., Min M., Reyniers M., Waters L. B. F. M., 2007a, A&A, 467, 1093
Deroo P., Acke B., Verhoelst T., Dominik C., Tatulli E., van Winckel H., 2007b, A&A, 474, L45
Dopita M. A., Sutherland R. S., 2000, ApJ, 539, 742
Ercolano B., Barlow M. J., Storey P. J., Liu X.-W., 2003, MNRAS, 340, 1136
Gerhard O., Arnaboldi M., Freeman K. C., Kashikawa N., Okamura S., Yasuda N., 2005, ApJ, 621, L93
Gerhard O., Arnaboldi M., Freeman K. C., Okamura S., Kashikawa N., Yasuda N., 2007, A&A, 468, 815
Gonçalves D. R., Magrini L., Leisy P., Corradi R. L. M., 2007, MNRAS, 375, 715
Guerrero M. A., Manchado A., 1996, ApJ, 472, 711
Howarth I. D., 1983, MNRAS, 203, 301
Iben I. Jr, Kaler J. B., Truran J. W., Renzini A., 1983, ApJ, 264, 605
James F., 1998, MINUIT Reference Manual 94.1. CERN, Geneva
Leisy P., Dennefeld M., 2006, A&A, 456, 451
Liu X.-W., Storey P. J., Barlow M. J., Clegg R. E. S., 1995, MNRAS, 272, 369 (LSBC)
Liu X.-W., Storey P. J., Barlow M. J., Danziger I. J., Cohen M., Bryce M., 2000, MNRAS, 312, 585
Liu X.-W., Luo S.-G., Barlow M. J., Danziger I. J., Storey P. J., 2001, MNRAS, 327, 141
Liu Y., Liu X.-W., Barlow M. J., Luo S.-G., 2004, MNRAS, 353, 1251
Liu X.-W., Barlow M. J., Zhang Y., Bastin R. J., Storey P. J., 2006, MNRAS, 368, 1959
Lodders K., 2003, ApJ, 591, 1220
Meaburn J., Walsh J. R., Clegg R. E. S., Walton N. A., Taylor D., Berry D. S., 1992, MNRAS, 255, 177
Meixner M., McCullough P., Hartman J., Son M., Speck A., 2005, AJ, 130, 1784
Mendoza C., 1983, in Flower D. R., ed., Proc. IAU Symp. 103, Planetary Nebulae. D. Reidel Publishing Co., Dordrecht, p. 143
Mesa-Delgado A., Esteban C., García-Rojas J., 2007, preprint (arXiv:0710.1285)
Morisset C., Stasińska G., Peña M., 2005, MNRAS, 360, 499
O'Dell C. R., Balick B., Hajian A. R., Henney W. J., Burkert A., 2002, AJ, 123, 3329
O'Dell C. R., Henney W. J., Ferland G. J., 2007, AJ, 133, 2343
Peimbert M., Peimbert A., Ruiz M. T., Esteban C., 2004, ApJS, 150, 431
Péquignot D., Baluteau J.-P., 1994, A&A, 283, 593
Péquignot D., Tsamis Y. G., 2005, A&A, 430, 187
Péquignot D., Walsh J. R., Zijlstra A. A., Dudziak G., 2000, A&A, 361, L1
Péquignot D., Amara M., Liu X.-W., Barlow M. J., Storey P. J., Morisset C., Torres-Peimbert S., Peimbert M., 2002, in Henney W. J., Franco J., Martos M., Peña M., eds, Rev. Mex. Astron. Astrofis. Ser. Conf. Vol. 12, Ionized Gaseous Nebulae. UNAM, Mexico, p. 142
Péquignot D., Liu X.-W., Barlow M. J., Storey P. J., Morisset C., 2003, in Kwok S., Dopita M., Sutherland R., eds, Proc. IAU Symp. 209, Planetary Nebulae: Their Evolution and Role in the Universe. Astron. Soc. Pac., San Francisco, p. 347
Rubin R. H. et al., 2002, MNRAS, 334, 777
Saviane I., Exter K. M., Tsamis Y. G., Gallart C., Péquignot D., 2008, A&A, submitted
Stasińska G., Szczerba R., 2001, A&A, 379, 1024
Sterling N. C., Dinerstein H. L., Kallman T. R., 2007, ApJS, 169, 37

Storey P. J., 1994, A&A, 282, 999
Storey P. J., Hummer D. G., 1995, MNRAS, 272, 41
Tsamis Y. G., 2002, PhD thesis, Univ. London
Tsamis Y. G., Barlow M. J., Liu X.-W., Danziger I. J., Storey P. J., 2003a, MNRAS, 338, 687
Tsamis Y. G., Barlow M. J., Liu X.-W., Danziger I. J., Storey P. J., 2003b, MNRAS, 345, 186
Tsamis Y. G., Barlow M. J., Liu X.-W., Storey P. J., Danziger I. J., 2004, MNRAS, 353, 953
Tsamis Y. G., Walsh J. R., Pequignot D., Barlow M. J., Liu X.-W., Danziger I. J., 2007, The Messenger, 127, 53
Weingartner J. C., Draine B. T., Barr D. K., 2006, ApJ, 645, 1188
Wesson R., Liu X.-W., Barlow M. J., 2005, MNRAS, 362, 424
Wesson R., Barlow M. J., Liu X., Storey P. J., Ercolano B., De Marco O., 2008, MNRAS, 383 1639
Zeippen C. J., Le Bourlot J., Butler K., 1987, A&A, 188, 251
Zijlstra A. A., Gesicki K., Walsh J. R., Péquignot D., van Hoof P. A. M., Minniti D., 2006, MNRAS, 369, 875

APPENDIX A: LINEAR REGRESSION ANALYSIS

In Table A1 the parameters of the fits discussed in Section 5 are detailed.

Table A1. Parameters of least-squares regression analysis discussed in Section 5: A – intercept, B – slope, r – correlation coefficient, σ – standard deviation, and Points – number of data points fitted. Values in parentheses are exponents of base 10.

Diagnostics	A	B	r	σ	Points
		NGC 6153			
O^{2+}/H^+ CEL versus T_e([O III])	2.25(−3) ± 2.00(−5)	−1.99(−7) ± 2.20(−9)	−0.98	0.57	296
ADF(O^{2+} λ4649) versus T_e([O III])	−58.2 ± 1.70	7.39(−3) ± 1.90(−4)	0.92	0.82	296
ADF(O^{2+} λ4089) versus T_e([O III])	−96.7 ± 3.70	0.012 ± 4.11(−4)	0.86	2.2	295[a]
C^{2+}/H^+ ORL versus T_e([O III])	−9.56(−3) ± 3.79(−4)	1.33(−6) ± 4.19(−8)	0.88	2.2	295
O^{2+}/H^+λ4649 ORL versus T_e([O III])	−9.13(−3) ± 7.66(−4)	1.42(−6) ± 8.40(−8)	0.70	1.2	296
O^{2+}/H^+λ4089 ORL versus T_e([O III])	−2.34(−2) ± 1.56(−3)	3.15(−6) ± 1.72(−7)	0.73	2.8	291[a]
C^{2+}/H^+ ORL versus O^{2+}/H^+λ4649 ORL	6.82(−5) ± 8.13(−5)	0.645 ± 0.021	0.87	2.3	294
C^{2+}/H^+ ORL versus O^{2+}/H^+λ4089 ORL	6.47(−4) ± 6.86(−5)	0.347 ± 0.013	0.85	2.4	290[a]
O^{2+}/H^+λ4649 ORL versus O^{2+}/H^+ CEL	6.72(−3) ± 1.80(−4)	−6.46 ± 0.39	−0.69	1.3	296
O^{2+}/H^+λ4089 ORL versus O^{2+}/H^+ CEL	1.15(−2) ± 3.81(−4)	−14.1 ± 0.82	−0.71	2.8	291[a]
C^{2+}/H^+ ORL versus O^{2+}/H^+ CEL	5.16(−3) ± 9.72(−5)	−5.87 ± 0.20	−0.86	2.4	295
O^{2+}/H^+ CEL versus He^{2+}/He	5.45(−4) ± 5.77(−6)	−1.36(−3) ± 4.48(−5)	−0.87	1.5	296
C^{2+}/H^+ ORL versus He^{2+}/He	1.72(−3) ± 3.35(−5)	9.83(−3) ± 3.58(−4)	0.85	2.5	295
ADF(O^{2+} λ4649) versus He^{2+}/He	4.62 ± 0.15	53.1 ± 1.90	0.86	1.1	295
ADF(O^{2+} λ4089) versus He^{2+}/He	5.17 ± 0.24	87.4 ± 3.20	0.85	2.3	293[a]
O^{2+}/H^+λ4649 ORL versus He/H	−0.0127 ± 0.0015	0.125 ± 0.011	0.55	1.5	296
O^{2+}/H^+λ4089 ORL versus He/H	−0.0321 ± 0.0031	0.282 ± 0.024	0.57	3.3	289[a]
C^{2+}/H^+ ORL versus He/H	−0.0118 ± 0.0010	0.109 ± 0.007	0.68	3.4	295
ADF(O^{2+} λ4649) versus He/H	−54.2 ± 4.90	476 ± 37.9	0.59	1.6	296
ADF(O^{2+} λ4089) versus He/H	−105 ± 9.90	882 ± 75.8	0.57	3.6	289[a]
C^{2+}/H^+ ORL versus c(Hβ)	−5.50(−4) ± 4.57(−4)	3.03(−3) ± 3.94(−4)	0.54	1.9	148[a]
ADF(O^{2+} λ4649) versus c(Hβ)	−8.86 ± 3.28	18.0 ± 2.84	0.47	1.0	147[a,b]
ADF(O^{2+} λ4089) versus c(Hβ)	−19.4 ± 4.55	31.8 ± 3.90	0.55	1.9	147[a,b]
T_e([O III]) versus c(Hβ)	7530 ± 248	1693 ± 211	0.56	1.2	146[a,b]
He^{2+}/He versus c(Hβ)	−0.167 ± 0.026	0.253 ± 0.023	0.68	2.0	147[b]
He^+/H^+ versus He^{2+}/H^+	0.128 ± 3.41(−4)	−0.673 ± 0.022	−0.87	0.45	292[a,b]
		NGC 7009			
O^{2+}/H^+ CEL versus T_e([O III])	1.63(−3) ± 1.52(−5)	−1.23(−7) ± 1.47(−9)	−0.98	3.1	294
ADF(O^{2+} λ4649) versus T_e([O III])	−26.2 ± 1.40	3.05(−3) ± 1.41(−4)	0.78	2.5	296
ADF(O^{2+} λ4089) versus T_e([O III])	−50.8 ± 2.40	5.78(−3) ± 2.34(−4)	0.82	2.0	293[a]
C^{2+}/H^+ ORL versus T_e([O III])	−3.23(−3) ± 4.23(−4)	4.08(−7) ± 4.06(−8)	0.66	1.6	135[b]
O^{2+}/H^+λ4649 ORL versus T_e([O III])	−9.48(−3) ± 9.88(−4)	1.08(−6) ± 9.48(−8)	0.70	1.6	135[b]
O^{2+}/H^+λ4089 ORL versus T_e([O III])	−8.56(−3) ± 8.72(−4)	1.13(−6) ± 8.49(−8)	0.62	2.0	293[a]
C^{2+}/H^+ ORL versus O^{2+}/H^+λ4649 ORL	7.50(−5) ± 3.23(−5)	0.519 ± 0.018	0.86	1.8	296
C^{2+}/H^+ ORL versus O^{2+}/H^+λ4089 ORL	3.11(−4) ± 3.31(−5)	0.230 ± 0.011	0.78	2.2	293[a]
O^{2+}/H^+λ4649 ORL versus O^{2+}/H^+ CEL	4.78(−3) ± 2.81(−4)	−8.70 ± 0.811	−0.68	1.6	135[b]
O^{2+}/H^+λ4089 ORL versus O^{2+}/H^+ CEL	6.10(−3) ± 2.53(−4)	−8.41 ± 0.694	−0.58	2.0	293[a]
C^{2+}/H^+ ORL versus O^{2+}/H^+ CEL	2.15(−3) ± 1.22(−4)	−3.27 ± 0.350	−0.63	1.6	135[b]
O^{2+}/H^+ CEL versus He^{2+}/He	4.39(−4) ± 2.90(−6)	−4.22(−4) ± 1.64(−5)	−0.84	7.9	289
C^{2+}/H^+ ORL versus He^{2+}/He	7.39(−4) ± 6.37(−5)	1.36(−3) ± 3.10(−4)	0.35	1.9	135[b]
ADF(O^{2+} λ4649) versus He^{2+}/He	1.19 ± 0.53	19.3 ± 2.57	0.55	2.6	135[b]
ADF(O^{2+} λ4089) versus He^{2+}/He	5.78 ± 0.28	15.9 ± 1.62	0.50	3.0	293[a]
O^{2+}/H^+λ4649 ORL versus He/H	−4.79(−4) ± 4.64(−4)	0.0201 ± 0.0040	0.28	2.5	294
O^{2+}/H^+λ4089 ORL versus He/H	−6.38(−3) ± 1.11(−3)	0.0819 ± 0.0096	0.45	2.3	290[a]
C^{2+}/H^+ ORL versus He/H	−3.13(−4) ± 2.88(−4)	0.0115 ± 0.0025	0.26	3.4	295

Table A1 – *continued*

Diagnostics	A	B	r	σ	Points
ADF(O^{2+} λ4649) versus He/H	−19.5 ± 2.01	214 ± 17.5	0.58	3.3	295
ADF(O^{2+} λ4089) versus He/H	−38.5 ± 3.90	409 ± 34.0	0.58	2.9	293[a]
He^{+}/H^{+} versus He^{2+}/H^{+}	0.110 ± 3.64(−4)	−0.789 ± 0.018	−0.93	0.86	293[a]
		NGC 5882}			
O^{2+}/H^{+} CEL versus T_e([O III])	1.71(−3) ± 4.52(−5)	−1.34(−7) ± 4.72(−9)	−0.89	8.2	204
ADF(O^{2+} λ4649) versus T_e([O III])	−5.39 ± 0.87	7.92(−4) ± 9.09(−5)	0.52	1.0	202
ADF(O^{2+} λ4089) versus T_e([O III])	−21.8 ± 2.62	2.70(−3) ± 2.74(−4)	0.58	1.8	197[a]
C^{2+}/H^{+} ORL versus T_e([O III])	−3.55(−4) ± 2.06(−4)	8.75(−8) ± 2.16(−8)	0.27	1.8	203
O^{2+}/H^{+} λ4649 ORL versus T_e([O III])	−6.16(−4) ± 3.85(−4)	1.60(−7) ± 4.05(−8)	0.27	1(−4)	203
O^{2+}/H^{+} λ4089 ORL versus T_e([O III])	−2.21(−3) ± 1.13(−3)	4.07(−7) ± 1.19(−8)	0.24	1.8	190[a]
C^{2+}/H^{+} ORL versus O^{2+}/H^{+} λ4649 ORL	1.56(−4) ± 2.98(−5)	0.347 ± 0.031	0.61	1.5	203
C^{2+}/H^{+} ORL versus O^{2+}/H^{+} λ4089 ORL	5.13(−4) ± 1.90(−5)	−0.0164 ± 0.0109	−0.11	1.9	196[a]
O^{2+}/H^{+} λ4649 ORL versus O^{2+}/H^{+} CEL	1.37(−3) ± 1.12(−4)	−1.07 ± 0.260	−0.28	1(−4)	203
O^{2+}/H^{+} λ4089 ORL versus O^{2+}/H^{+} CEL	2.95(−3) ± 3.15(−4)	−3.01 ± 0.739	−0.28	1.82	193[a]
C^{2+}/H^{+} ORL versus O^{2+}/H^{+} CEL	7.13(−4) ± 5.95(−5)	−0.547 ± 0.140	−0.26	1.8	203
O^{2+}/H^{+} CEL versus He^{2+}/He	4.47(−4) ± 2.97(−6)	−8.48(−4) ± 7.62(−5)	−0.68	14	148[c]
C^{2+}/H^{+} ORL versus He^{2+}/He	4.88(−4) ± 7.70(−6)	−1.44(−4) ± 1.73(−4)	−0.06	1.9	199
ADF(O^{2+} λ4649) versus He^{2+}/He	1.95 ± 0.04	5.62 ± 0.87	0.42	0.31	200
ADF(O^{2+} λ4089) versus He^{2+}/He	3.52 ± 0.13	12.6 ± 3.19	0.27	2.7	200[a]
O^{2+}/H^{+} λ4649 ORL versus He/H	2.23(−3) ± 2.94(−4)	−0.012 ± 0.003	−0.30	1(−4)	203
O^{2+}/H^{+} λ4089 ORL versus He/H	4.87(−3) ± 1.22(−3)	−0.029 ± 0.011	−0.18	2.6	203[a]
C^{2+}/H^{+} ORL versus He/H	9.29(−4) ± 1.72(−4)	−4.12(−3) ± 1.59(−3)	−0.18	1.9	203
C^{2+}/H^{+} versus $c(H\beta)$	4.76(−4) ± 8.1(−6)	1.38(−5) ± 1.61(−5)	0.06	1.9	203[a]
ADF(O^{2+} λ4649) versus He/H	7.07 ± 0.84	−45.4 ± 7.80	−0.38	0.31	203
ADF(O^{2+} λ4089) versus He/H	12.9 ± 2.46	−83.1 ± 22.7	−0.25	2.2	197[a]
He^{+}/H^{+} versus He^{2+}/H^{+}	0.108 ± 3.27(−4)	−1.13 ± 0.071	−0.75	1.4	201[a]

[a]Corresponding plot not shown.
[b]Fit only for the inner nebula (coloured red) data points; see the text for details.
[c]Fit only for the outer nebula (coloured blue) data points; see the text for details.

This paper has been typeset from a TEX/LATEX file prepared by the author.